FINITE ELEMENT ANALYSIS OF MACHINING LIGHTWEIGHT SYNTACTIC FOAMS

by

Kevin Koshy Thomas

A Thesis presented to the Faculty of the
American University of Sharjah
College of Engineering
In Partial Fulfillment
of the Requirements
for the Degree of

Master of Science in
Mechanical Engineering

Sharjah, United Arab Emirates

April 2021

Declaration of Authorship

I declare that this thesis is my own work and, to the best of my knowledge and belief, it does not contain material published or written by a third party, except where permission has been obtained and/or appropriately cited through full and accurate referencing.

Signed……………………………………………………………………….

Date……………………… 06/05/2021 …………………………

Approval Signatures

We, the undersigned, approve the Master's Thesis of Kevin Koshy Thomas.

Thesis Title: Finite Element Analysis of Machining Lightweight Syntactic Foams

Date of Defense: 21-Apr-2021

Name, Title and Affiliation	Signature
Dr. Sathish Kannan Assistant Professor, Department of Mechanical Engineering Thesis Advisor	
Dr. Maen Abdelqader Alkhader Associate Professor, Department of Mechanical Engineering Thesis Committee Member	
Dr. Rajiv Selvam Associate Professor, Department of Mechanical Engineering Manipal Academy of Higher Education, Dubai Campus Thesis Committee Member	
Dr. Mamoun Abdel-Hafez Head Department of Mechanical Engineering	
Dr. Lotfi Romdhane Associate Dean for Graduate Affairs and Research College of Engineering	
Dr. Sameer Al-Asheh Interim Dean College of Engineering	
Dr. Mohamed El-Tarhuni Vice Provost for Graduate Studies Office of Graduate Studies	

Dedication

To my family…

Abstract

Aluminium alloys reinforced with hollow alumina microsphere syntactic foams possess superior physical and mechanical properties such as improved stiffness, peak compressive strength and total specific energy absorption. However, due to the inherent abrasive and brittle nature of the hollow alumina microspheres, syntactic foams bring two key machining issues in the form of poor machinability and surface integrity. This research focuses on understanding the physics behind chip formation during machining metal syntactic foams through development of a 2D finite element (FE) model which will enable to predict cutting forces using AdvantEdge FE software. To elucidate and explain the failure mechanisms in the form of hollow ceramic microsphere fracture and plastic deformation of the aluminium matrix which contributes to generation of cutting forces, a 2D ABAQUS/Explicit FE model is developed. Cutting tests were conducted on the aluminium syntactic foam with varying cutting velocity and undeformed chip thickness. Two different volume fractions (10% and 20%) with varying average hollow microsphere sizes were used in the validation trials. From the FE results, it is shown that the increase in cutting speed results in reduction of cutting force due to thermal softening of matrix alloy. However, the measured cutting force increase with increasing undeformed chip thickness is primarily due to increasing chip load. Increase in shear strength of the material is noticed with increasing volume fraction and finer hollow microsphere size which contributes to a higher magnitude of cutting force. A greater number of fractured hollow microspheres were involved in two-body and three-body tool abrasion on the rake face thereby increasing the cutting force. The finite element cutting force simulations is compared with the measured values for different cutting conditions. The AdvantEdge FE model shows comparable results with the validation experiments within an error of 15%.

Keywords: *Hollow alumina microspheres; matrix; cutting force; abrasion.*

Table of Contents

List of Figures

List of Tables

List of Abbreviations

Bubble	Hollow microsphere
EHM	Equivalent homogenous model
FEM	Finite element model
JC	Johnson and Cook
MMC	Metal matrix composite
MMSF	Metal matrix syntactic foam
PCD	Polycrystalline diamond

Chapter 1. Introduction

1.1. Preamble

A composite material refers to a system of materials composed of two or more materials that are not soluble in each other on a standard scale. Take the example of concrete, which contains a combination of cement, sand, stones, and water. If the material involves microscopic composition (molecular level), then, for metals, it is known as an alloy. Normally, composite materials consist of two phases: [1] One phase is called the matrix phase, and the other is the reinforcement phase. The matrix holds the reinforcement to obtain the desired mechanical properties of the new material. Composite materials have improved strength that is superior to that of the matrix or reinforcement alone.

Composites are lighter in weight than wood and steel. Their lightness is crucial for increasing fuel efficiency when they are used in automobiles and airplanes. Composites can be manufactured to be stronger than aluminum or steel. While a metal has uniform strength in all directions, composites can be stronger in one particular direction. Some natural materials may be strong and heavy, whereas others may be weak and light. However, composites can be tailored to be both strong and light. This particular attribute is the reason that such materials are used to build airplanes. Today, it is well known that, out of all structures, the one made up of composites has a high strength-to-weight ratio [2]. Composites can resist the corrosion caused by weather and, particularly, by harsh chemicals that erode other materials. They are an excellent choice for the storage of chemicals. In outdoor conditions, they can withstand harsh climates and extreme changes in temperature. Composites can also absorb high amounts of impact energy, such as that created by the force of a bullet or the shockwaves of explosions. Because of this, these materials are used for making bulletproof vests and panels. Given composites' flexibility, designers have the freedom to create any shape they want regardless of how complex it is. The surface of the composites can also be designed to obtain any finish or texture, from smooth to rough. In addition, composites can be used for near-net-shape manufacturing, which reduces the amount of finishing work needed. Composites can also last longer compared to other materials and, thus, require very little maintenance. Finally, they can also offer low thermal conductivity.

Based on the matrix phase, composites can be classified into three types: (a) polymer matrix composites (PMCs), (b) metal matrix composites (MMCs), and (c) ceramic matrix composites (CMCs) [1]. Among these, MMCs are commonly used for many applications in the industry due to their remarkable strength and wear resistance. A notable example is of the cylinder liners used in internal combustion engines. The excellent wear resistance of MMC materials is due to the reinforcements of hard abrasive ceramics present in the matrix [3].

Two of the most notable MMCs used in certain industries are aluminum matrix composites and magnesium matrix composites. Aluminum matrix composites are mainly used in aircraft, aerospace, and automobile applications due to their excellent physical and mechanical properties [4]. The reinforcements incorporated into the aluminum matrix improve the composites' stiffness, specific strength, wear, creep, and fatigue properties as compared to conventional materials. SiC-reinforced Al MMCs have greater wear resistance as compared to Al_2O_3-reinforced Al MMCs and are therefore an excellent choice of materials for manufacturing brake drums. A SiC-reinforced Al MMC has three times the strength-to-weight ratio of mild steel [5]. Further, the composite has higher wear resistance than a B_4C-reinforced MMC. Previous studies have proven that increasing the volume fraction of Al_2O_3 reinforcement reduces the fracture toughness of Al MMC. It is also possible to increase the thermal conductivity and reduce the thermal expansivity of MMC using diamond fiber as reinforcement for Al MMCs. Hence, we can see the numerous capabilities of the Al MMCs that used for a variety of applications.

Magnesium matrix composites represent another potential material that can be used for aerospace and defense applications. This is owing to their low density in addition to their desirable mechanical and physical properties [6]. When compared to SiC-reinforced Al MMCs, the magnesium MMC, reinforced with SiC, provides better creep and wear resistance. Further, Al_2O_3 reinforcement helps improve the wettability and bonding strength of Al MMCs. If we increase the percentage of reinforcements, we can increase the density, hardness, and ultimate tensile strength of the resultant composite [7].

Machining is one of the crucial manufacturing processes. The development of various machining operations can be traced back to the Industrial Revolution [8].

Machining is commercially and technologically significant for several reasons: (a) Plastics and plastic composites are also machinable. However, ceramics pose difficulties in this regard due to their high hardness and brittleness. (b) Typical geometric shapes, such as flat planes and round holes, can be created through machining, while irregular shapes, such as screw threads and gear teeth, can be created by providing variations in the tool shapes and paths. (c) Components that have dimensions with very close tolerances can be produced through machining. (d) Machining can be used to produce a smooth surface finish, while certain abrasive processes can achieve even better finishes. The popularity of machining justifies the importance of understanding the mechanics of metal cutting. This understanding is needed to develop novel machine tools and optimize machining techniques. It is also required for producing products made from new types of engineering materials, which are traditionally difficult to manufacture owing to their enhanced mechanical and physical traits [9].

Machining MMCs is a challenging task when compared to machining homogenous metals in the industry. This is mainly true when hard ceramic reinforcements are present in MMCs. During machining, the reinforcement particles rub against the rake face. As a result, the tool surface gets severely damaged, which leads to tool wear [10]. Excessive tool wear, in turn, leads to various types of damage, i.e. debonding and fracturing, to a huge number of reinforcement particles. There are also some complications related to the mechanics of chip formation of MMCs, which further complicates the machining process. This is due to the interaction between the tool, the matrix, and the reinforcement [11]. Thus, the machining of MMCs is a challenging process. It is considerably difficult to optimize the process parameters to attain the preferred tool-life, surface integrity, and metal removal rate.

To overcome these limitations, many novel improvements have been made in computer technologies to enable scientists to attain proper clarity regarding machining via numerical simulations. Finite element modelling is a technique that is currently being used to achieve a wide range of knowledge related to the different details of the machining process, such as the formation and separation of chips, the damage that occurs at the subsurface level of the workpiece, and the chip–tool interactions [12]. The essential requirement for any finite element model is to obtain the details about the

15

materials constitutive behavior. The constitutive equations illustrate a stress–strain relationship that relies on strain hardening, strain rate, and temperature. The result predicted by the equation is correct only if we understand how the material behaves under machining. Constitutive equations are reliable tools for analyzing the relationship between the workpiece and the machining aspects of the cutting process. Sometimes, alterations, such as to the size of reinforcement microspheres or the volume fraction of the microspheres, are made to the equations to make the predicted values comparable to the experimental values.

With regard to MMCs, based on the reinforcement particle, there are three types (see Figure 1): (a) continuous fiber MMCs, (b) short fiber MMCs, and (c) particle-reinforced MMCs. In fiber MMCs, the classification is based on the aspect ratio of the length of the fiber to the cross-sectional dimension. If the aspect ratio is significantly high, the material is considered a continuous fiber MMC. Short fibers usually refer to the fibers that have a low aspect ratio. In the case of particulate reinforcement, the aspect ratio is approximately equal to one. Hence, the shape of a particle can be spherical, cubic, platelet-like, or any regular or irregular geometric structure [13]. The MMCs that we are interested in are a special type of hollow microsphere-reinforced MMCs called metal matrix syntactic foams (MMSFs).

(a)　　　　　　　　　　　　　　　　(b)

(c)
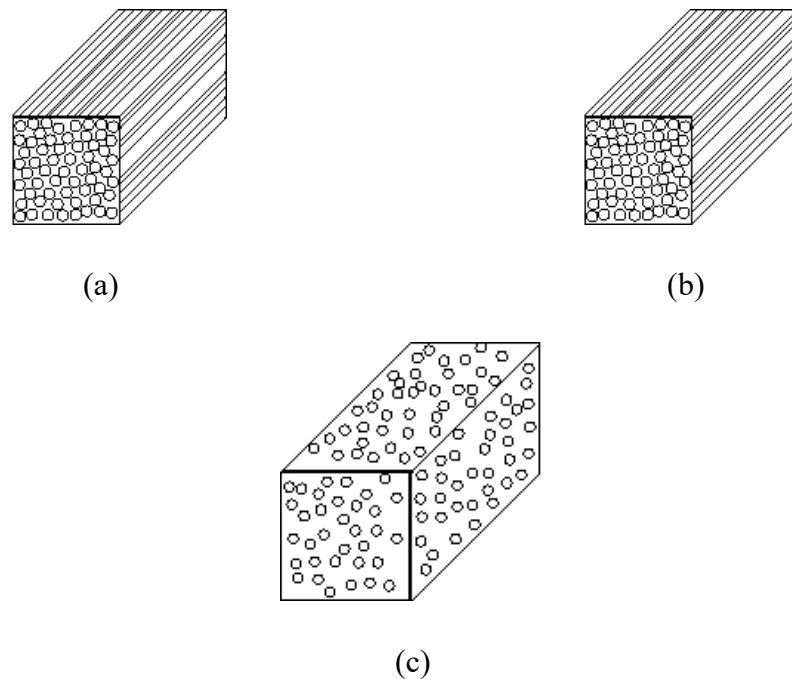
Figure 1: Types of MMCs with respect to reinforcements: (a) continuous fiber, (b) short fiber, and (c) particle reinforced [1]

Syntactic foam is a binary material that consists of preformed hollow microspheres and a matrix, which binds the two, to produce a material that possesses the required strength and stiffness and is lighter than monolithic materials [14]. The characteristics of the microspheres and the matrices directly affect the thermal, electrical, and mechanical characteristics of syntactic foams. Studies have shown that the highest possible volume percentage of microspheres in MMSFs is 65%. Moreover, due to the hollow microspheres, these foams have 50% porosity, which helps save weight when compared to conventional materials.

The use of syntactic foams offers benefits such as lower fuel consumption and increased payload capacity. The composition of the foams can be tailored based on our interests. Syntactic foams are used in marine applications due to their low moisture absorption and buoyancy properties. They can also be used to insulate deep-water pipes, in the hulls of boats, and to manufacture soccer balls.

Based on the cellular structure, syntactic foams can be classified into two types: (a) open-cell foams and (b) closed-cell foams. In this thesis, the focus will be on closed-cell syntactic foams [15]. Under normal circumstances, closed-cell foams, shown in Figure 2, will have more density and strength in comparison to open-cell foams.

Figure 2: Closed-cell syntactic foams [14]

Chapter 2. Background and Literature Review

2.1.   Introduction

This chapter will provide a brief explanation of the literature associated with metal matrix syntactic foams, their physical and mechanical properties, and the constitutive models and force models of the foams. As there are closed-cell and open-cell types of syntactic foams, this chapter will also discuss the finite element modelling of the associated cellular metals and that of the syntactic foams.

2.2.   Metal Matrix Syntactic Foams

Rohatgi et al. [16] defined metal matrix syntactic foams as a unique type of composite that includes microspherical voids inside the matrix such that the resultant encircling porous zone, which is inside the thin shell of the microsphere, provides low density without significantly affecting the mechanical properties of the material. When compressing these syntactic foams, a large plateau can be seen in the stress-strain graph. The size of this plateau can be adjusted by controlling the thickness of the wall of the microsphere, the volume fraction of the microspheres, the average size of the microspheres, and the total energy that the microspheres can absorb upon compression.

These metallic foams have a great stiffness-to-weight ratio and a reversible, seemingly elastic region [17]. Due to this, they can be used in light structures. However, when compared to the base metal, the other mechanical properties of the metal foams are quite inferior. Therefore, they are limited to applications where strength is not a primary design criterion. To overcome this issue, a novel method of adding porosity to the foams was developed. This method involves the usage of hollow microspheres as fillers. The surrounding porosity inside these stiff and strong microspheres, which are inside a metal matrix, leads to a material that can have a higher modulus and strength than those of the homogeneous metals. This new material or composite is referred to as a MMSF. In addition to the weight reduction, controlling the porosity size of the spherical shape of the microspheres helps in attaining high energy absorption under compression.

Ceramic microspheres, which have a negligible thickness, are essential for manufacturing lightweight foams. Due to this, these are readily used. They provide high

stability to the material in terms of dimensions by reducing thermal expansion. There are two types of hollow microspheres: [16]

- Micro balloons
- Fly ash Cenospheres

Micro balloons are hollow ceramic microspheres of high quality. They undergo several quality control processes, such as pressurization, to separate the weaker and defective particles and select only the intact low-density particles. The popular materials for producing ceramic micro balloons are glass, alumina, zirconia, and carbon.

Fly ash cenospheres are produced during coal combustion and are a by-product of industrial waste. One of the most challenging task is to separate cenospheres from the by-products, which involves significant costs. However, incorporating cenospheres in metals can lead to a considerable amount of savings on raw materials and can thus lead to reducing pollution. The problem with using these particles is that they contain trace amounts of certain toxins, such as As, Cd, Pb, and Zn. The leaching of these toxins from these particles is also a concern. These issues have to be addressed when using these particles for the manufacturing of cenosphere-filled syntactic foams.

2.3.   Characteristics of Metal Matrix Syntactic Foams

A notable feature of MMSFs is their excellent compressive characteristics. To understand these characteristics, we need to understand how the syntactic foam fails under compression, as shown in Figure 3 and in the stress-strain graph shown in Figure 4. During initial compression, the microspheres that are located near the middle of the foam will collapse. The corresponding stress is called the peak strength of the foam, as evident in the graph. Further, the stress drops while an increase in strain, and a fairly lower constant value of stress, called the plateau strength, exists for a certain range of strain until the stress starts to increase exponentially [18]. During the stress drop and the plateau region, the matrix alloy will densify, and the remaining microspheres will collapse until we reach a point where the foam is fully densified. The strain at this point is referred to as densification strain, which helps us identify the start of the stress increase. The area of the plot of the compression test up to the densification strain will help us determine the maximum amount of energy the foam will absorb during impact.

There are some notable past studies that made observations while compressing the syntactic foam. Broxtermann et al. [19] performed a compressive test on a highly porous pearlite metal syntactic form (PMSF). Porous expanded pearlite was used for the hollow microspheres due to its lower cost, and A356 aluminum alloy was the material of the matrix for the PMSF. The foam was manufactured using a compaction and infiltration method. While plotting the stress–strain curve, the authors found that the compressive proof strength in the stress plateau relies on the struts of the matrix within the PMSF. As observed from the quasi-elastic gradient of the plot, they concluded that an increase in the matrix volume fraction increases foam density. This, in turn, leads to thicker matrix struts that result in higher stiffness. Besides, a higher matrix volume fraction leads to better specific energy absorption capabilities. Compared to the existing MMSFs, it was shown that the high porosity PMSF exhibits a comparatively high value of stress plateau.
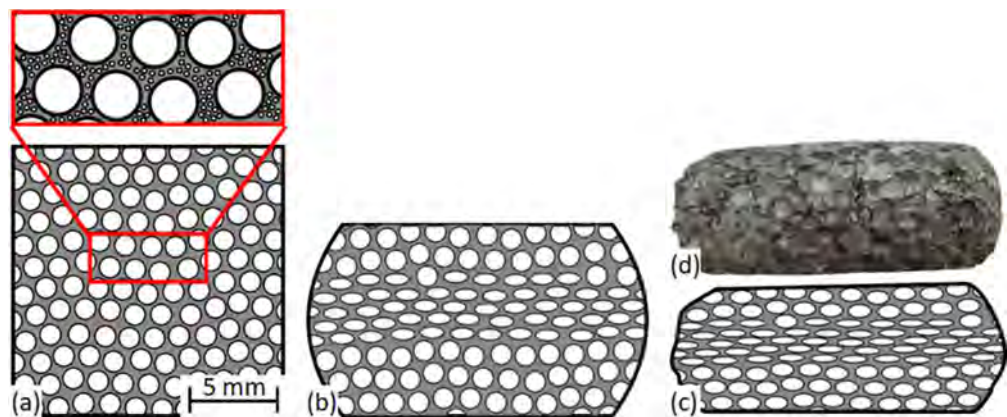
Figure 3: Stages of the failure mechanism of the syntactic foam under the compression test (assuming aspect ratio = 1) [18]

Magnesium alloys have a lower density than aluminum alloys and provide greater energy absorption. This was demonstrated by David et al. [20], who detailed the mechanical characteristics of magnesium alloy syntactic foam. The foam was synthesized using the sub-atomic pressure infiltration technique. They noted from the stress–strain graph that the foam containing the smallest alumina hollow microspheres exhibited a good amalgam of peak strength and specific energy absorption. Moreover, the peak strength exceeded the elastic limit of the magnesium alloy, indicating a transfer of load from the matrix to the microspheres as a result of a strong bond between the Mg-AZ91D alloy and the alumina microspheres. This was observed through the scanning electron microscope. Last, the peak stress, fairly level stress, and toughness

were found to rise with an increase in the wall thickness-to-diameter ratio of the hollow microsphere. Since this proportion increased with the reduction of the spheres' diameter, foams that have finer hollow microspheres result in better performance. These observations further corroborate those of the previous study.
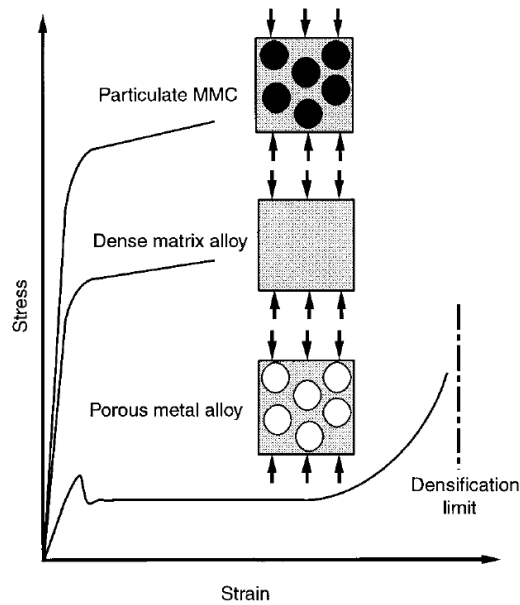
Figure 4: Comparisons between the compressive test plot features of syntactic foams, dense alloys, and cellular metals [21]

2.4.   Material Modelling for Metal Matrix Syntactic Foams

The properties that are relevant when designing a MMSF include (a) density, (b) peak stress, (c) plateau stress, (d) densification strain, (e) toughness, and (f) specific energy absorption. In this section, certain notable constitutive models for the peak compressive strength or proof strength of MMSFs have been discussed.

Kiser et al. [21] created a model to examine the hollow microsphere of MMSFs under both unconstrained compression, which is in one direction, and constrained die compression types of loadings. The model was based on Gurson's constitutive law for void metals to provide additional information regarding the material response of the MMSFs. The law is extremely useful for explaining the flow behavior of higher plastic strains due to constrained conditions. A comparison was made between this particular type of foam and the conventional metal foams. Experimental studies have shown that syntactic foams can exhibit strengths that are much greater than the matrix alone.

21

Although the model considered the wall thickness-to-radius ratio of the microspheres to calculate the volume fraction of the microspheres, it failed to consider the compressive strength of the microspheres.

This problem was averted when Wu et al. [22] created a modified model that included the relationship between the peak strength of the microspheres, the radius ratio of the microsphere, and the peak strength of the matrix. The peak strength of the microspheres is calculated by an equation in terms of the wall strength of the microsphere and the void volume fraction of the microsphere. While taking the load separation effect of microspheres in MMSFs [23] into account, they calculated the peak strength of the foam using the combined effect of the matrix and the microspheres [22]. They were able to conclude that the syntactic foams with a lower microsphere void volume fraction and the smallest microsphere size will have the highest peak strength.

A further modification was made by Mondal et al. [24] to include the volume fraction of the voids in the sphere wall in the analysis. The model was developed with the same load-partitioning concept [23] used in the previous study. The values of this model were agreeable with the experimental values with fairly good accuracy. These models address the elastic properties of MMSFs, which is good for the design of structural components. However, these models rely heavily on empirical constants. Hence, they will not be suitable for MMSFs with varying compositions.

Ferguson et al. [25] developed the model that predicts the peak stress of MMSFs subjected to unconstrained compression. This model described the plastic deformation up to the point of densification based on the energy absorption system design. The model considered two types of plastic deformation: Type A—spheres that got fractured before additional matrix yielding—and Type B—matrix yielding at the same time as the sphere gets fractured. The authors compared the predicted values with the experimental values, the results of which were agreeable with regard to peak stress.

2.5.   Finite Element Model

In addition to the force models discussed above, a few numerical models will be discussed, which have been built to understand the simulation of the chip formation for MMSFs and to validate the values of the models with the experiments. We will also discuss the finite element model (FEM) of machining metal foam.

2.5.1. Metal matrix composites. Although we have talked about the development of force models in the previous section, we still need to visually understand the formation of the chip and its interaction with the tool in the context of MMSFs. These illustrations will also provide further insights regarding the slight variation in the cutting force values when comparing the model and the experiments. Thus, Pramanik et al. [26] investigated the behavior of MMCs, which was mainly focused on the tool–particle interaction and the residual stresses developed during 2-D cutting, using finite element simulation. The investigation also explored how the stress/strain fields were developed and analyzed particle fractures and debonding to provide more clarity about machining MMSF. The software used was the 10th version of ANSYS/LS-DYNA. In the boundary conditions of the FEM, the Lagrangian formulation was used in the material continuum for the development of the plane-stress model. The arrangement of the particles was adjusted in such a way that the rows of particles would be inclined with the cutting edge, as illustrated in Figure 5. This facilitated the analysis of the particle interaction with the rake face and the cutting edge. The tool was considered to be rigid and advanced horizontally into the foam at a low cutting velocity. In material modelling, a temperature-independent plastic kinematic material model was used for the matrix alloy.

According to the ANSYS/LS-DYNA [26] manual, the yield stress for this model is given by the following equation:

$$\sigma_y = \left[1 + \left(\frac{\dot{\varepsilon}}{C}\right)^{1/P}\right]\left(\sigma_0 + \beta E_P \varepsilon_p^{eff}\right) \tag{1}$$

Based on this study, the interaction between the tool and the particles was classified into three scenarios: (a) particles along the cutting path, (b) particles above the cutting path, and (c) particles below the cutting path, as shown in Figure 6. A chip separation criterion was used in the model, which was available in the software. For tool–chip interaction, the Coulomb friction model was used for considering the friction effect between the tool and the workpiece. From the results, they were able to achieve a qualitative agreement between the FEM and the experiments available in the literature. They were able to conclude that the stress distribution around the foam and the interaction between the microspheres and the tool are the cause of the microsphere fracture and debonding. The newly generated surface was found to be under

23

compressive residual stresses, and the rapid wear of the tool was attributed to the sliding of the pull-out microspheres over the cutting edge and the rake face of the tool during chip flow.
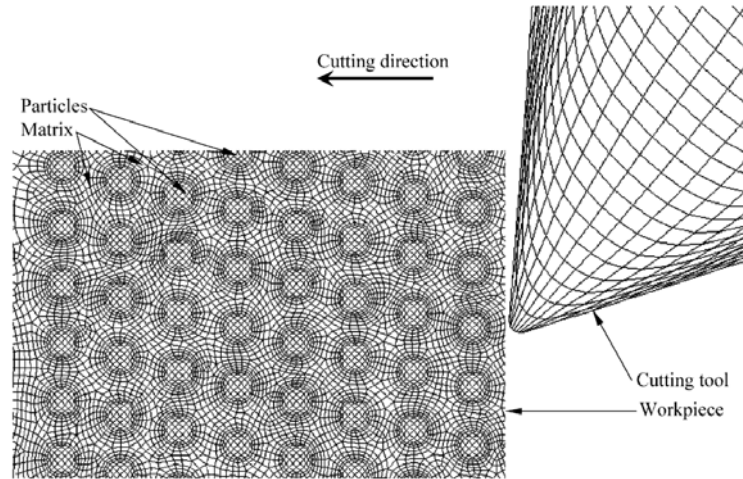
Figure 5: MMC machining simulation [26]
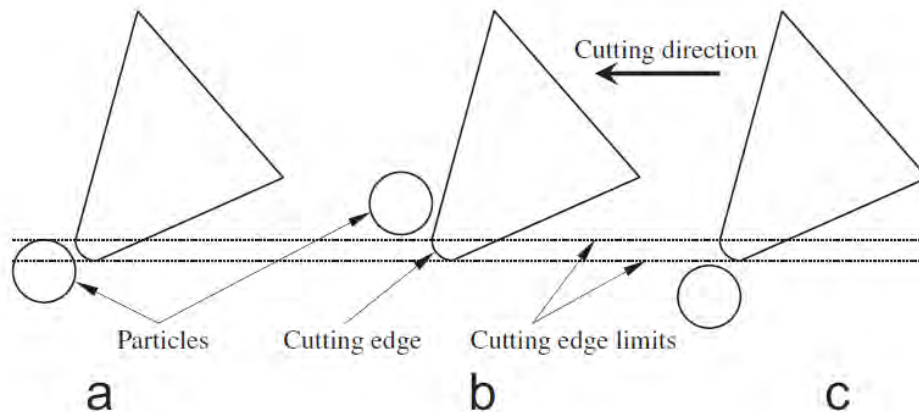
Figure 6: Location of the particle with respect to the cutting path: (a) along, (b) above, and (c) below the cutting path [26]

Pramanik et al. [11] explicitly explained the microsphere fractures and pull-outs in MMSFs in terms of primary, secondary, and tertiary shear zones. The constraints were the same as those of the previous study that was discussed, and the 10th version of the ANSYS/LS-DYNA software was used for developing a two-dimensional plane-stress FEM. For the material model, the authors chose a temperature-independent plastic kinematic model. The main difference in this study, when compared to the previous discussion, is that the microsphere was considered as a plastic kinematic

material compared to the perfectly elastic material considered for the microspheres in the previous study. Moreover, the yield strength of the microsphere was very high, so its behavior was elastic until it fractured. They concluded that microsphere pull-outs and fractures occurred in secondary and tertiary shear zones and not in the primary shear zone during machining. The strain field is also maximum in the secondary and tertiary shear zones. The sharp-edged and fractured microspheres significantly contribute to tool wear, which further verifies the inferences of the previous study. The high-strain field in the tertiary shear zone results in strain hardening on the newly generated surface.

Qi et al. [27] developed a multi-phase-based model to understand the mechanics of chip formation during the machining of particle-reinforced composites. The effect of the tool–particle interaction on the cutting forces and the deformation and fracture of reinforcement particles were investigated. The finite element (FE) software used was ABAQUS/Explicit, and Johnson and Cook's constitutive model and damage models were utilized to provide the properties of and the fracture damage to the matrix. The maximum normal stress theory was used for describing the fracture of SiC particles. It was concluded that two types of particle fractures were present in the workpiece. One was caused by the direct contact of the cutting-edge radius with the particle, while the other was caused by the indirect tool–particle interaction through the matrix. The particle fracture is significantly influenced by the relative positions between the tool and particle, which also affects the surface finish. The cutting forces will reach the maximum value when the tool makes direct contact with the particle.

Umer et al. [28] constructed a FEM to understand the tool performance based on the development of temperature and stresses during the machining of aluminum-based syntactic foam using a PCD tool. The software they used was ABAQUS/Explicit with the Lagrangian formulation. Two kinds of models were developed: (a) FEM without cohesive elements and (b) FEM with cohesive elements. The former was used for the evaluation of temperature and stresses at varying cutting speeds and feeds, while the latter was used to monitor tool–particle interaction. For the material model, the Johnson and Cook constitutive model (Eq. (12)) was employed for the prediction of stress variation due to strain, strain rate, and temperature.

25

$$\sigma = (A + B\varepsilon^n)\left(1 + C\ln\left(\frac{\varepsilon}{\varepsilon_0}\right)\right)\left(1 - \left(\frac{T - T_r}{T_m - T_r}\right)^m\right) \tag{2}$$

The chip separation criterion was modelled based on Johnson and Cook's damage law. The tool–workpiece contact was modelled using a sliding–sticking friction model. From their analysis, the authors observed that bands of low and high shear strains were alternatively repeated, which qualitatively aligns with the experimental findings. They also observed high-stress regions around the rake face of the tool, as shown in Figure 7. This is due to the fact that a high number of hard microspheres were present in the region. A rise in feed rate was found to increase the size of this stress region. The effect of the cutting speed had a greater influence on cutting temperature when compared to the effect of the feed rate. There was an increase in tool stresses due to the sliding and rolling actions of the microspheres, which increased with an increase in the size of the microsphere and the cutting velocity.
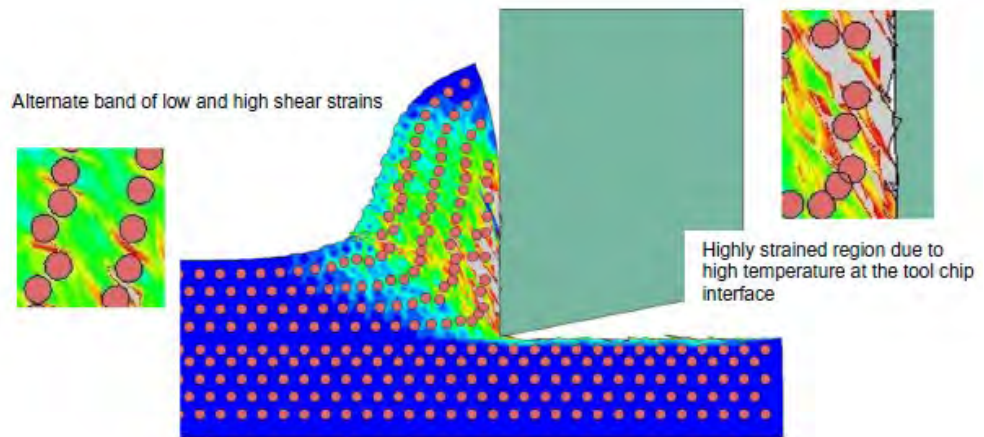
Figure 7: Chip formation with plastic strain contour. [28]

Elkhateeb et al. [29] developed a three-dimensional FE simulation based on a multi-scale heterogeneous model (MHM) to understand the chip formation behavior of titanium-based syntactic foam during conventional machining and laser-assisted machining (LAM). They also tried out an equivalent homogeneous model (EHM) as the FEM. However, the MHM-based simulations were able to accurately predict the high thrust forces due to the addition of the tool–particle interaction. In the EHM, the AdvantEdge™ software was used through a 3-D nose-turning model based on an updated Lagrangian design with continuous and adaptive meshing techniques. In the

MHM, the simulations were performed using ABAQUS/Temp-disp/Explicit. According to the study's conclusion, the MHM simulation showed that the high thrust forces that occur during the machining of the foam was due to the tool–particle interaction that occurred along the cutting path. The foam provided higher resistance to the penetration of particles into the machined surface during machining. This resulted in the thrust forces being higher than the cutting forces during conventional machining, Nevertheless, during LAM, there was a significant reduction in the thrust forces and the tool flank wear owing to the matrix becoming softer and a reduction in the strength of the interface between the matrix and the microspheres. Thus, the agreement between the experimental and the simulation results was found to be good.

Dou et al. [30] created an FE model for the drilling process on aluminum-based syntactic foams using an improved version of the constitutive model using ABAQUS/Explicit. The model was improved by including the volume fraction of the microspheres in the Johnson and Cook constitutive model. For the boundary conditions, a cone-like concave-shaped indentation was made on the workpiece surface to ensure stable drilling. For chip separation, Johnson and Cook's damage law was used, and the authors used Coulomb's law for the friction model. From the results, they found that the thrust force and torque from the FE values were within 11.04% and 20.6% of the errors, respectively. This happened due to three reasons: (a) the simulation model was simplified, (b) uneven occurrence of element error, and (c) heterogeneity of the foam.

Usama et al. [31] developed 2-D and 3-D FE models to simulate the orthogonal metal cutting of aluminum-based MMCs. The 2-D model was a heterogeneous micro-mechanics (MM) model, which was used for the study of the nature of MMC machining, while the 3-D model was an equivalent homogeneous-based model used for capturing the influence of the volume fraction of the particles. The difference between the EHM and MM-based models is that the former provides a reduced computational time. The MM model has a high computational cost due to very fine mesh that is used to handle the high deformation mechanism. The model is highly efficient with regard to the prediction of local variables, such as stress and temperature. Both the models are capable of measuring cutting forces and temperature with a reasonable degree of accuracy.

Qi et al. [32] developed a microstructure-based FE model for the investigation of the mechanism of chip formation and subsurface damage during the machining of a particulate type of MMC using ABAQUS/Explicit. The model used the improved version of the Johnson and Cook's constitutive model for simulating the behavior of the matrix alloy. The JC damage model was used to analyze the failure of the matrix, and the Rankine criterion and fracture energy cracking criterion were used to analyze the particle fracture. To reduce the computational cost, two models were created in the workpiece, namely the multi-phase (MP) model and the equivalent homogeneous model (EHM), such that the latter surrounded the former. From their analysis, the authors concluded that the depth of the cut affects the surface finish and cutting forces. The particle fracture was caused due to the high-stress concentrations and high strains in the shear zone created by the cutting edge of the tool. Further, serrated chips were formed due to the matrix deformation along the primary shear zone and a cluster of particles. The particle fractures also created cavities along the machined surface.

Xiangyu et al. [33] conducted a numerical study on an orthogonal metal removal mechanism for magnesium-based MMCs reinforced with solid nano-SiC particles. A ABAQUS/Explicit analysis was used to develop a 2-D FE model to simulate micro-machining while taking the effect of the cutting-edge radius into consideration. For the matrix, the Johnson and Cook constitutive equation and fracture equation were used. As for the fracturing of the SiC particles, brittle shear and brittle failure definitions were used. Based on the contour images, it was observed that the particles obstructed the flow of the matrix, thereby resulting in high-stress regions around the strained field. A continuous chip with serrations was created due to high-strain bands near the particles on the chip.

Usama et al. [34] investigated the different methods used for modelling the orthogonal machining of SiC particles reinforced with aluminum-based MMCs. The authors concluded that the elements are capable of simulating the particle debonding of the reinforcement particles from the matrix. A FE model with cohesive zone elements and a predefined cutting layer provided a better simulation of serrated chips and even revealed localized shear regions around the chip face. Hongmin et al. [35] created an FE model, while taking the cohesive zone elements into consideration, for the analysis of the micro-machining of aluminum MMCs reinforced with nano-sized SiC particles.

28

The matrix was based on the Johnson and Cook constitutive equation, and the brittle cracking model was used in the study. It was concluded, based on the simulation results, that the non-uniform interaction between the tool and the reinforcements existed due to the random arrangement of the SiC particles. This also led to the inhomogeneous distribution of stresses and irregular cutting force variations.

Most of the FE models developed considered the FE reinforcements to be spherical in shape. However, Rashid et al. [36] developed a novel FE model by assuming the SiC particles-reinforced aluminum matrix under orthogonal cutting to be oval in shape. The particles were randomly arranged in the matrix. The results indicated that the cutting force increased with an increase in the feed rate. Moreover, an increase in the feed rate reduced the type of chips created from spring-shaped coils to C-type chips. This also increased the radius of the chip curl and the number of chip curls. Finally, an increase in the shape of the oval-shaped particles increased the number of chip coils and reduced the radius of the chip curl.

2.5.2. Cellular metals. The machining of metal foams poses a challenge due to the resulting surface being irregular. Due to the limitations of the analytical and experimental methods, the FE is used as a suitable alternative for analyzing the chip formation mechanisms and the causes of the surface defects that result from the material removal of cellular metals. However, only a few of the FE models for metal foams are available. Silva et al. [37] built a mesoscopic FE model for simulating the chip formation process from cellular metals during machining. Further, 2-D machining tests were conducted for validating the FE values with experimental values. The open-cell cellular material was heat-resistant austenitic stainless steel. The ABAQUS/Explicit software was used for using the coupled temperature–displacement, three-node linear plane-strain elements for discretizing the model. The ductile damage model was the material separation model used in the simulation. From their results, the authors concluded that the material was initially separated due to a tension load acting on the struts and, finally, due to the shear load occurring closer to the nodes. The material was squeezed only at a negative rake angle with a lower cutting speed. Last, the model was found to be capable of simulating chip formation for metal foams.

Heidari and Yan [38] investigated the mechanism of material removal by performing ultra-precision surface flattening of the porous silicon with the help of

diamond turning. They also employed the FE simulations to assist their understanding of the change in the machining mechanism around the pores by investigating the cutting-stress field produced around a pore in porous silicon. The simulation software used was AdvantEdge[TM]. The cutting parameters values were the same as those used in the experiments. For material modelling, a pressure-sensitive Drucker–Prager constitutive model was used for silicon. As shown in Figure 8 (a), a large area of tensile stress was formed below the tool tip, which extended toward the pore. This sort of tensile stress leads to brittle fractures. Nevertheless, as seen in Figure 8 (b), there was only a small area of stress just below the tool tip, which is too low to initiate brittle fractures. Thus, the simulation results were found to be agreeable with the experimental results.
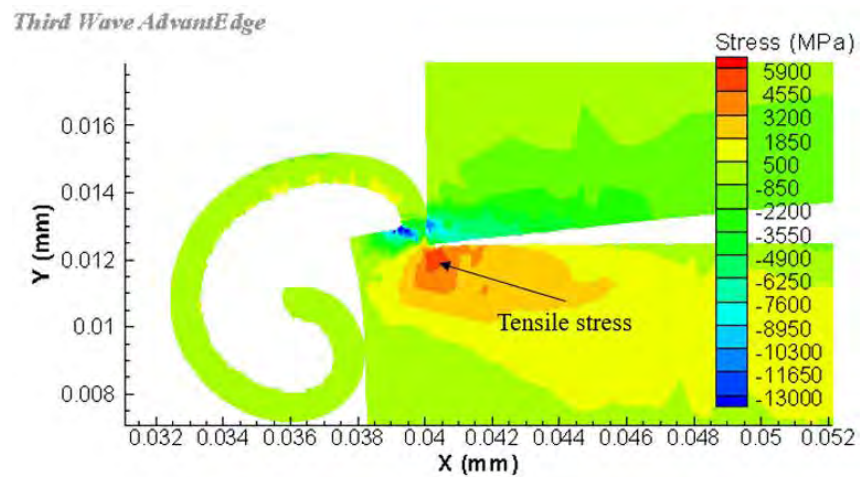
(a)
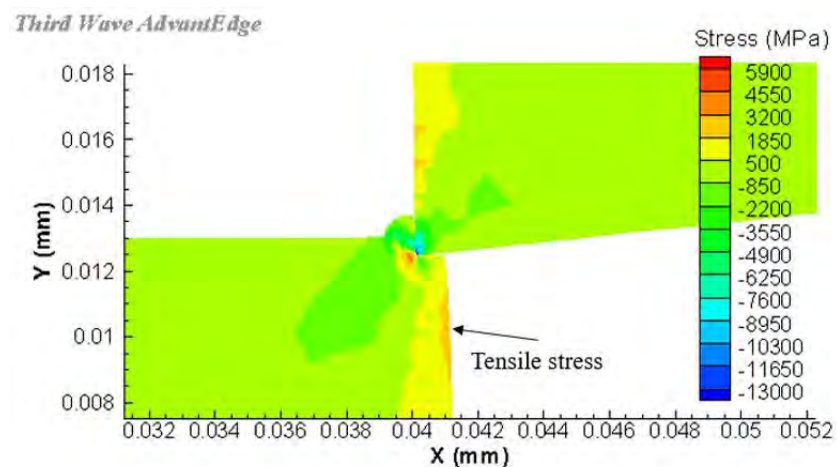
(b)
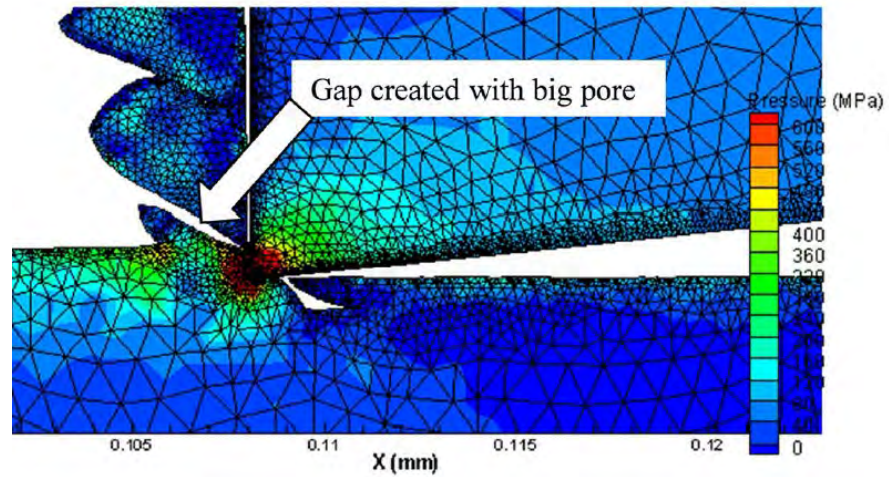
(c)
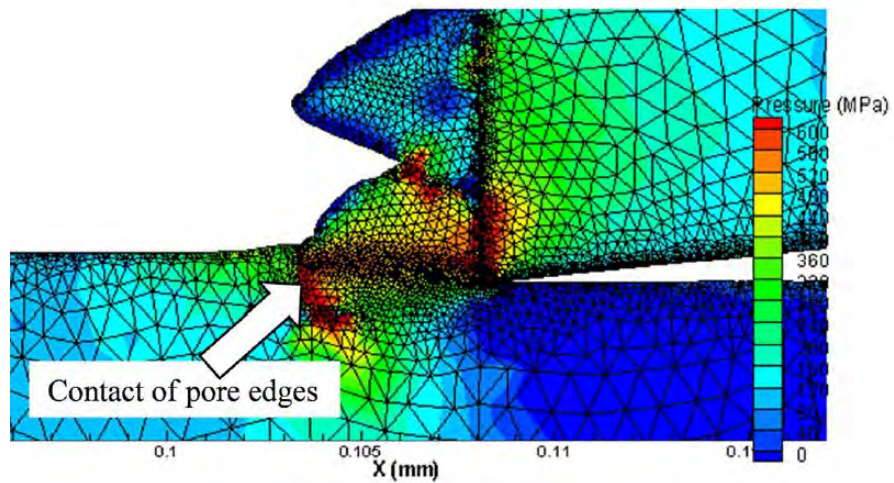
(d)

Figure 8: Stress distributions around a pore in (a), (b) porous silicon and (c), (d) porous titanium [38], [39]

Heidari and Yan [39] studied the chip formation mechanism and the surface texture during the precision machining of porous titanium. To understand these aspects, the simulation software AdvantEdge[TM] was used to simulate the chip formation of porous titanium. The material model used for the metal foam was the modified power-law constitutive model, which was already built into the software. From the simulations, the authors concluded that the presence of pores aided the elimination of the shear deformation of the foam, as shown in Figure 8 (c). In addition, a saw-toothed chip, the size of which relies on the location of the pore, was formed when machining porous titanium. Last, a welding phenomenon, seen in Figure 8 (d), was seen when the chip

moved toward the other side of the pore as the tool advanced toward the edge of the pore. This phenomenon also explained the negligible difference between the cutting force values of pure and cellular titanium.

Heidari et al. [40] analyzed the influence of the rake angle of the cutting tool on the stress distribution produced by the cutting edge and examined how this effect affects the brittle fracture around the pore. To simulate the chip formation of porous silicon, the AdvantEdge^{TM} software was used to better understand how the rake angle affects the material removal mechanism. The pressure-sensitive Drucker–Prager constitutive model was the material model used for silicon. From the simulation results, the authors inferred that high-stress areas were induced by the cutting edge if the rake angle was reduced. Tensile stresses were observed just below the cutting edge as the tool moved toward the pore edge. These stresses induced micro-crack propagation and, possibly, brittle fractures. At a zero rake angle, if the stresses were less than the tensile yield stress of silicon, it was that a brittle fracture will not occur. However, at a reduced rake angle, the fracture occurs even before the tool reaches the pore edge.

Silva et al. [41] developed a mesoscopic FE model to explicitly illustrate the chip formation and the mechanisms of damage that occur during the peripheral milling of cellular metals. The FE simulation program used was ABAQUS/Explicit. To discretize the program, coupled temperature–displacement, three-node linear plane-strain elements were used. The metal foam was a heat-resistant austenitic stainless-steel cellular material. Further, Johnson and Cook's empirical equation was used as the constitutive model for the FE simulation of metal foams. The ductile damage model was used for modelling material separation, while the Coulomb friction model was used for tool–workpiece interaction. Base on the simulation, the authors found that the temperature remained comparatively low (under 250° C) in comparison to the machining of monolithic stainless steel. The rise in temperature was found to be exclusively dependent on the heat generated from the plastic strain. This is because the primary and secondary deformation zone was completely absent and because the interaction between the workpiece and tool were negligible. The occurrence of material separation was found to only happen after a progressive increase in plastic strain as the cutting edge moved along the surface. The chip mainly consisted of small fragments of struts due to the relatively small feed. This simulation was carried out based on three

conditions: the use of a 2-D model instead of a 3-D one, the absence of geometrical defects, and the specific mechanical properties of the struts.

Chapter 3. Objective

Based on the inference from the literature review, in order to use syntactic foam in potential applications, there is a need to study the machinability of aluminum-based syntactic foams. The main objective of this thesis is to study the mechanics of chip formation during the machining of MMSFs. To achieve this objective, there are four main factors to be studied that affect the mechanics:

3.1.   Cutting Force

As the tool starts cutting the workpiece, the chip is formed by shear deformation along a plane called the shear plane. The failure of the workpiece starts from the cutting edge of the tool. Most of the mechanical energy is consumed in the shear plane due to the plastic deformation of the work material. The remaining energy is released in the form of heat due to the friction between the chip and the rake face and the friction between the flank face and the newly generated workpiece surface. Therefore, it is vital to estimate the material properties of the workpiece, its microscopic structure, and the arrangement of microspheres inside it. All of these factors need to be considered to analyze the causes of the generation of the cutting force during the machining of MMSFs, as we need to model the cutting force and, thereby, predict the type of chip formed.

3.2.   Effect of Process Parameters

In addition to the material behavior, the undeformed chip thickness, the width of the cut, and the cutting speed will likely affect the cutting forces generated while machining metal matrix foams. Moreover, the specifications of the tool will affect the generated forces. These specifications include the rake angle, relief angle, and edge radius. Last, the working condition of the tool will also affect the cutting force. For example, a blunt cutting edge will increase the cutting force as compared to a sharp cutting edge.

3.3.   Role of Hollow Microspheres

The shape (assumed to be spherical) and the average size of the microspheres will affect the compressive properties of the microspheres. This will, in turn, affect the overall shear strength of the MMSF. Moreover, the volume fraction of the microspheres

will affect the shear strength. If we know the shear strength, we can accordingly model the cutting force.

3.4. Chip Formation

Here, we will qualitatively validate the chip formed using numerical simulations. This is done to verify and understand the crack propagation formed in the chip during syntactic foam machining.

Chapter 4. Experiments

4.1. Work Material

The hollow alumina microspheres were obtained from Pacific Rundum Co., Ltd. Japan. These were used for squeeze casting cylindrical AA7075 and AA6061 aluminum syntactic foam billets for machining trials at Swamequip Ltd. India. The composition and physical properties of the hollow alumina microspheres used in this study are presented in Table 1. The microstructure of the AA7075 aluminum metal syntactic foam and its representative ceramic hollow microsphere are shown in Figure 9 (a)–(d). The microstructure of the AA6061 aluminum metal syntactic foam and its representative ceramic hollow microsphere are shown in Figure 10 (a) and (b).

Table 1:Composition and physical properties of the alumina microsphere reinforcements [42]

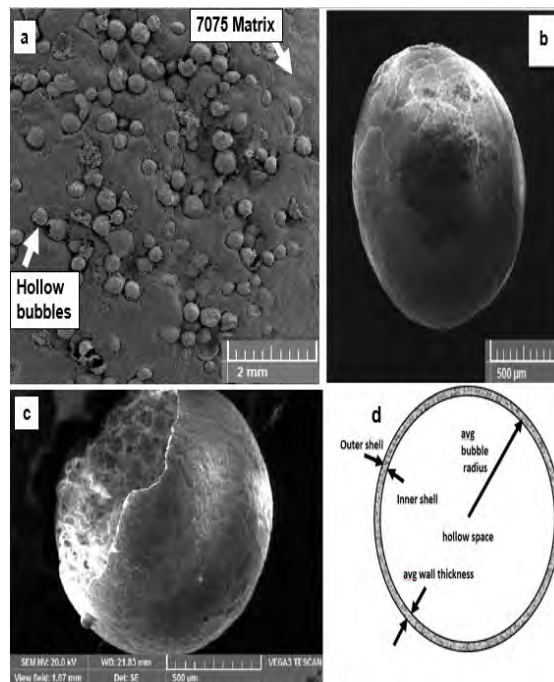| Avg. bubble size (mm)	Al_2O_3	Fe_2O_3	Cao	SiO_2	Na_2O	Bulk density (g/cm^3)	Porosity(%)	Avg. wall thickness (µm)	Crush strength (MPa)
0.3–0.6	99.7	0.003	0.01	0.025	0.26	1.8	85	0.035 to 0.085	120–130

Figure 9: (a) AA7075 syntactic foam; (b) hollow alumina microsphere; (c) fractured microsphere; (d) specification of hollow microsphere [42]
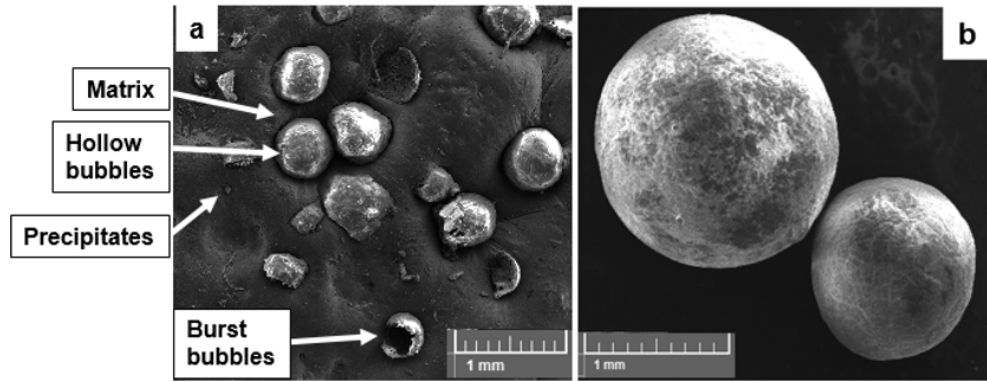
Figure 10: (a) AA6061-based syntactic foam; (b) hollow alumina microsphere [43]

4.2. Experimental Setup

Cutting experiments were carried out on two matrix types of aluminum (AA6061 and AA7075) reinforced with hollow ceramic alumina microspheres for validating the developed numerical cutting force model for MMSFs. Two different volume fractions and sizes of the ceramic microspheres were used in the experiments. Thus, in total, there were three types of workpieces. The Johnson–Cook parameters for both AA6061 and AA7075 syntactic foams are listed in Table 2 and Table 3, respectively. The orthogonal cutting tests were conducted using a three-axis CNC lathe. All the tests were conducted in a dry environment with different cutting parameters of uncut chip thickness (0.02 mm, 0.07 mm, 0.15 mm, and 0.2 mm), cutting speeds (25 m/min, 50 m/min, and 100 m/min), reinforcement volume fractions (10% and 20%), and average microsphere sizes (0.3 mm and 0.6 mm). The cutting experiments and the process parameters are summarized in Table 4 and Table 5, respectively. A KISTLER™ 9129AA three-channel dynamometer was used along with a multichannel charge amplifier type 5080 to measure the machining forces. The chips were collected after each test to measure the shear angle. All tests were conducted twice to ensure the repeatability of the experiment, and the average values of the measurements were noted.

Table 2: Values of the Johnson–Cook model for the AA6061 matrix used in this study [43]

Matrix	A (MPa)	B (MPa)	n	C	m	Reference Strain Rate	T_m (° C)	T_r (° C)
AA6061	150	450	0.39	0.012	0.5	1	652	20

Table 3: Values of the Johnson–Cook model for the AA7075 matrix used in this study [42]

Matrix	A (MPa)	B (MPa)	n	C	m	Reference Strain Rate	T_m (° C)	T_r (° C)
AA7075	170	658	0.53	0.019	0.32	1	635	20

Table 4: Experiment conditions for the AA6061-based syntactic foams [43]

Test Factors		
Matrix	AA6061	
Reinforcement	Hollow alumina	Micro microsphere closed-cell foam
Bubble volume fraction	(Vol. %)	10%, 20%
Cutting speed	m/min	25, 50, 100
Undeformed chip thickness	mm	0.02, 0.07, 0.15, 0.2
Width of cut	mm	3 mm
Cutting insert	Sandvik™	Coated carbide inserts
Coolant	Dry cutting	

Table 5:Experiment conditions for the AA7075-based syntactic foams [42]

Test Factors		
Matrix	AA7075	
Reinforcement	Hollow Alumina	Micro microsphere closed-cell foam
Bubble volume fraction	(Vol. %)	10%, 20%
Cutting speed	m/min	25, 50, 100
Undeformed chip thickness	mm	0.07, 0.15, 0.2
Width of cut	mm	3 mm
Cutting insert	Kennametal™	Coated carbide inserts
Coolant	Dry cutting	

Chapter 5. Finite Element Modelling and Methodology

In this chapter, the numerical simulation software used for modelling will be discussed.

5.1. AdvantEdge^{TM}

This software was developed by Third Wave Systems, USA. A 2-D EHM was developed to simulate the machining of AA6061- and AA7075-based syntactic foams. AdvantEdge^{TM} combines advanced FE technology with a user-friendly graphic interface designed specifically for metal cutting simulations. This software is used for predicting machining forces and temperature.

5.1.1. Geometry modelling and meshing.
For tool modelling, the appropriate inserts used in the experiment are shown in Table 4 and Table 5. The tools used were made from a carbide material. The cutting edge radius was taken as 0.035 mm and 0.03 mm for the AA6061- and AA7075-based syntactic foams, respectively. Fully automatic adaptive re-meshing of the FE mesh was applied at the primary and secondary shear zones to ensure the accuracy of the simulation. For the AA6061-based syntactic foam workpiece, eight different rectangular cross-section-type jobs were used, whose lengths varied from 3 mm to 9.5 mm, depending on the required convergence, and whose height was 2 mm. For the AA7075-based syntactic foam workpiece, seven different rectangular cross-section-type jobs were used, whose length varied from 9.3 mm to 15 mm, depending on the required convergence, and whose height was 2 mm. To adhere to the boundary conditions, the workpieces were mechanically constrained at its base. The boundary conditions for the cutting speed and the feed rate of the cutting tool were imposed on the reference point on the cutting edge of the tool. The software has a tri-element-mesh option for the meshing of the workpiece and tool. The meshing for the tool and workpiece is shown in Figure 11. For the effective reduction of computation cost, the minimum and maximum mesh size of the workpieces were taken as 20 μm and 100 μm, respectively. The workpieces had a number of nodes, ranging between 72,000 and 300,000 depending on the machining parameters.
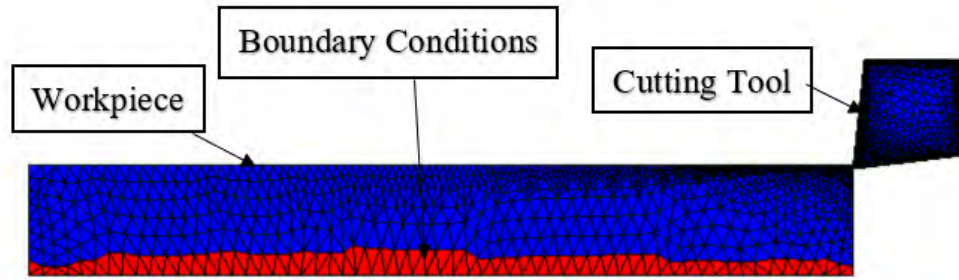
Figure 11: Meshing and boundary conditions in AdvantEdge^{TM}

5.1.2. Parameters for constitutive model. The material relationships between stress and strain are described by the Johnson–Cook model under the conditions of large deformation, high strain rate, and elevated temperatures. Given its simplicity, and as it requires less effort to estimate the material constants, this model has been widely employed by many researchers to predict the flow behavior of materials. The mechanical behavior of AA6061- and AA7075-based foam materials are highly anisotropic. However, in this study, to simplify the material modelling of this highly heterogeneous material system, the material model has been approximated as being equivalent to a homogeneous model. The material constants for the AA6061 and AA7075 matrices have been presented in Table 2 and Table 3, respectively. The physical, thermal, and elastic properties for the syntactic foams are provided in Table 6 and Table 7. The coefficient of thermal expansion was assumed to be 2.52E-5 K^{-1} [44]. The chip separation criteria are an essential part of the orthogonal machining simulation. Normally, there are two types of techniques used for chip separation: the node-splitting technique and the element deletion technique. In the case of the node-splitting method, a chip separation plane is predefined, and a separation criterion is applied. There are two types of separation criteria, which normally are geometrical and physical. Since the geometrical ones do not have physical implications, they are considered inferior in comparison to the physical ones. This makes the physical ones much more suitable. The physical criteria make use of the critical value of a physical quantity for the estimation of the start of the chip separation. Based on the input value of the reference strain rate present in the JC yield stress equation, the damage parameters for node-splitting for chip separation are calculated using an in-built function in the software.

40

Table 6: Properties of the AA6061-based syntactic foams [43]

Material	Vol. %	Thermal Conductivity (W/m-K)	Specific Heat (J/kg-K)	Density (g/cm³)	Elastic Stiffness (GPa)
AA6061/Hollow Alumina	10%	155	890	2.55	4
	20%	150	880	2.51	4.5
	Large bubble – 10%	145	870	2.52	3.8

Table 7:Properties of the AA7075-based syntactic foams [42]

Material	Vol. %	Thermal Conductivity (W/m-K)	Specific Heat (J/kg-K)	Density (g/cm³)	Elastic Stiffness (GPa)
AA7075/Hollow Alumina	10%	133	900	2.63	2.7
	20%	130	860	2.5	2.9
	Large bubble – 10%	125	850	2.69	2.65

5.1.3. Friction modelling. Many of the FEMs available for machining employ the classical friction theory that is based on Coulomb's law. The friction coefficient between the tool and the workpiece can have significant effects on the simulation results. The friction sliding force is directly proportional to the applied normal load. The ratio of these two forces represents the coefficient of friction, which is constant for all the secondary shear zones formed between the chip and cutting tool for different machining parameters. AdvantEdge^{TM} uses a friction coefficient defined by Coulomb friction in the following equation:

$$f_{fr} = \mu N \tag{3}$$

where, f_{fr} is the normal force exerted between the surfaces, μ is the coefficient of friction, and N is the resulting force due to friction. The coefficient of friction, which varies from 0.8–1.0, is used in the simulation.

5.1.4. Simulation results. The cutting force results of the simulation analysis are validated through a comparison with the experimental values. Moreover, the model provides an overall understanding of how the foam behaves under machining, which includes the interactions between the tool and the particles, the tool and the matrix, and

the particles and the matrix. The analysis also provides a clear explanation about closed-cell foams and their effects on machining forces. More importantly, the results help us understand which parameters (i.e. bubble size and volume fraction of the microspheres) affect the cutting force. Last, we will compare the surface of the chip from the simulation with that obtained from the experiment.

5.2. ABAQUS/Explicit

A 2-D multi-phase model is developed to simulate the orthogonal cutting of the AA6061-based syntactic foam to understand the physics behind the chip formation mechanism. The simulation was conducted using ABAQUS/Explicit.

5.2.1. Geometry modelling and meshing. To model the tool, a cutting insert 2 mm in height was modelled. The tool was elastic and was assumed rigid. The tool was constrained to allow movement only along the negative x-axis direction. During machining operation, a great amount of heat was generated, which affects the material's properties. Therefore, this analysis uses mechanical and thermal analyses, which were found to affect each other and were obtained simultaneously. The matrix and the hollow particles contained quad-dominated coupled temperature–displacement (CPE4RT) elements, and the tool consisted of rigid quad-dominated elements. For the boundary conditions of the workpiece, the base and the left side of the workpiece were fixed. For the thermal boundary conditions, the tool and the workpiece were maintained at 20° C. During machining, the cutting speed of the tool was set to 50 m/min, and an uncut chip thickness of 0.3 mm is used. For workpiece meshing, a mesh size of 10 μm was used. For the tool meshing, a minimum mesh size of 10 μm and a maximum mesh size of 98 μm were used. The number of elements in the tool and the workpiece were 6921 and 22,059, respectively. The meshing and boundary conditions for the tool and the workpiece are shown in Figure 12.

5.2.2. Parameters for constitutive model. To understand the chip formation mechanics, the multi-phase material model was developed, which helped us analyze the interactions between the hollow bubbles and the matrix, the matrix and the tool, and the hollow bubbles and the tool. For the matrix, the Johnson–Cook material model was used, in which the flow stress relies on the strain, strain rate, and temperature. The constants for the model were obtained from the stress–strain–temperature tests, and their values are given in Table 2. The properties of the matrix, the hollow bubbles, and
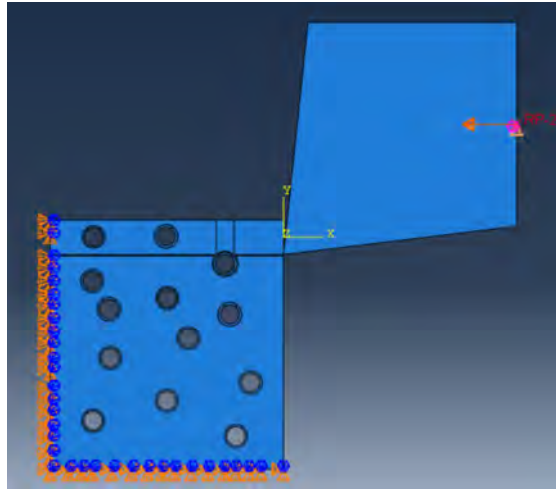
(a)
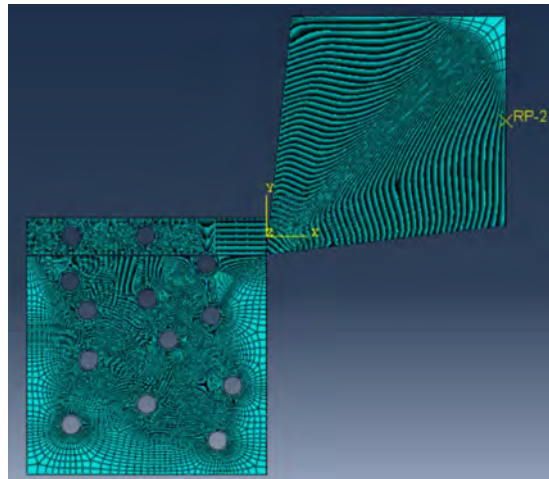
(b)

Figure 12: (a) Boundary conditions and (b) meshing in ABAQUS

the tool are provided in Table 8, Table 9, and Table 12, respectively. The chip separation criteria are an essential part of the orthogonal machining simulation. The material starts to fail when the damage parameter becomes equal to 1. The Johnson–Cook damage model for the aluminum matrix was used to calculate the equivalent strain at failure. The failure model coefficients are presented in Table 10. As for the damage evolution, the displacement at failure was 0.005 mm. For the fracture of the hollow microspheres, whose values are mentioned in Table 9, the brittle cracking criterion was used. The displacement-to-failure measurement for the hollow microsphere was 0.0001

mm. The retention type of brittle shear was used for the hollow microspheres, as shown in Table 11.

Table 8: Properties of AA6061 [44], [45]

Thermal Conductivity (W/m-K)	Thermal Expansion (1/K)	Inelastic Heat Fraction	Specific Heat (J/kg-K)	Young's Modulus (GPa)	Poisson's Ratio	Density
155	2.52E-5	0.9	890	68	0.33	2.7E-9

Table 9: Properties of the hollow alumina microspheres [46], [47]

Failure Stress (MPa)	Mode 1 Fracture Energy	Thermal Conductivity (W/m-K)	Density (g/cm^3)	Young's Modulus (GPa)	Poisson's Ratio	Thermal Expansion Coefficient (1/K)	Specific Heat (J/kg-K)
135	0.03	1.5	1.8	80	0.231	4.6E-6	755

Table 10: Johnson and Cook damage parameters for AA6061 [44]

D1	D2	D3	D4	D5
-0.77	1.45	-0.47	0	1.6

Table 11: Brittle shear for hollow microsphere [44]

Shear retention factor	Crack opening strain
1	0
1	1

Table 12: Properties of the cutting tool [48], [49]

Thermal Conductivity (W/m-K)	Coefficient of Thermal Expansion (1/K)	Young's Modulus (GPa)	Poisson's Ratio	Density (g/cm^3)	Specific Heat (J/kg-K)
110	5.5E-6	700	0.31	15.6	39.8

5.2.3. Friction modelling. The friction models provided in ABAQUS/Explicit are mostly used for simple problems. The most basic one is the classical Coulomb friction model. The shear stress limit, τ_{cri}, at which surfaces begin to slide with respect to each other, was calculated by the following equation:

$$\tau_{cri} = \mu p \qquad (4)$$

where, μ is the coefficient of friction, and p is the normal pressure. In this simulation, a penalty friction formulation without an elastic slip and softened tangential behavior was used. The values for the coefficient of friction and frictional shear stress were found to be 0.15 MPa and 50 MPa, respectively [44].

Chapter 6. Results and Discussion

This chapter will discuss the results from the FE, which were compared with the experimental results. The chapter will also explain the mechanism of chip formation.

6.1. Effect of Cutting Speed

The effect of the cutting speed on the generated forces during the machining of the two syntactic foams, AA6061 and AA7075, both reinforced with 10% volume of hollow alumina microspheres, is shown in Figure 13 (a) and (b). The measured cutting forces were found to decrease with an increase in the cutting speed by an order of up to 150 N. The FE model predictions were within an error margin of 15% (Figure 14 (a)–(c) and Figure 15(a)–(c)). Increasing the cutting speed caused the thermal softening of the aluminum matrix, which resulted in decreased cutting forces (Figure 14(d)–(f) and Figure 15(d)–(f)). This phenomenon of matrix softening enables the interfacial cracks to propagate and widen at a faster pace, causing the microspheres to get debonded and released out of the matrix. This results in the formation of a large volume of voids and pits on the machined surface, as a greater proportion of ceramic microspheres are pulled out of the matrix during cutting operation. The shear force (F_s) and the friction force (F) were analytically calculated using Merchant equations [8] which are shown below:

$$F = F_c \sin \propto + F_t \cos \propto \tag{5}$$

$$F_s = F_c \cos \phi - F_t \sin \phi \tag{6}$$

where F_c and F_t are the cutting force and the thrust force predicted through finite element. α and ϕ are the rake and the friction angles respectively.

6.2. Effect of Undeformed Chip Thickness

Figure 16 (a) and (b) illustrate the effect of undeformed chip thickness on the generated cutting forces while cutting syntactic foams with a 10% volume fraction of hollow microsphere reinforcements whose matrices are AA6061 and AA7075, respectively. An increase in the undeformed chip thickness results in an increase in the cutting forces generated primarily due to an increase in the chip load on the cutting tool (Figure 17 (a)–(d) and Figure 18 (a)–(c)). An increase in the cutting forces is also attributed to the presence of a larger volume fraction of hollow ceramic microspheres
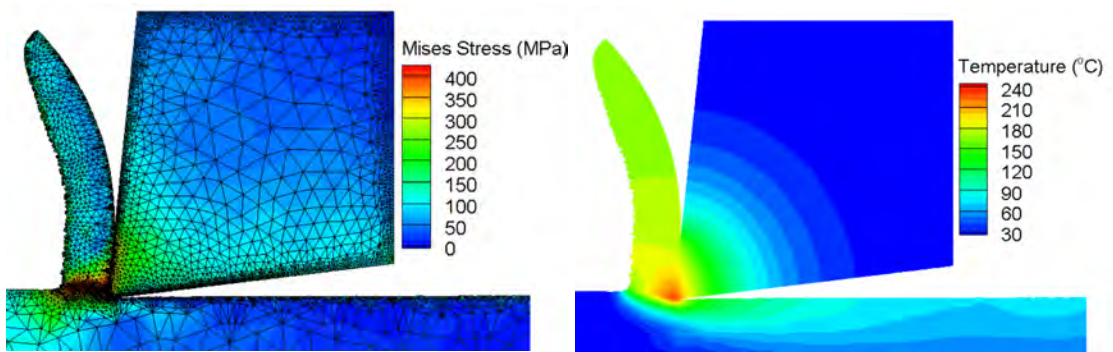
46
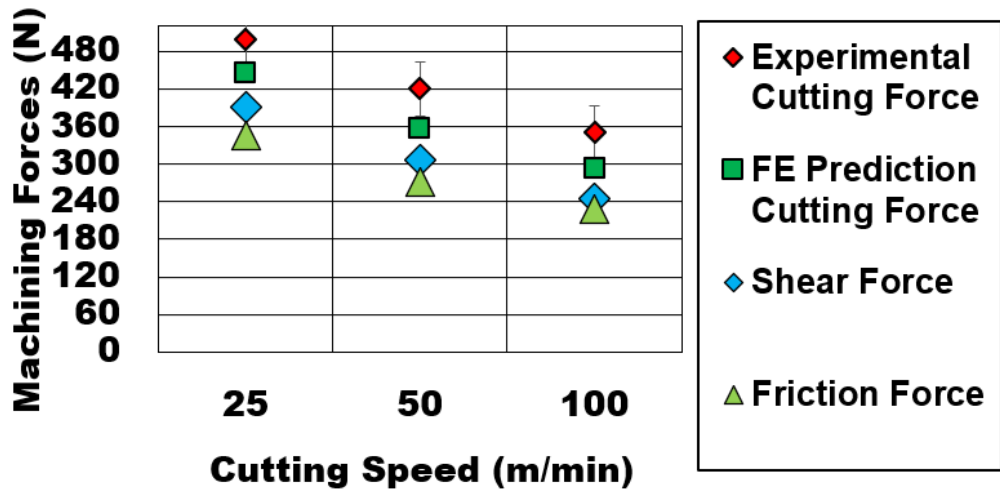
(a) AA6061 syntactic foam
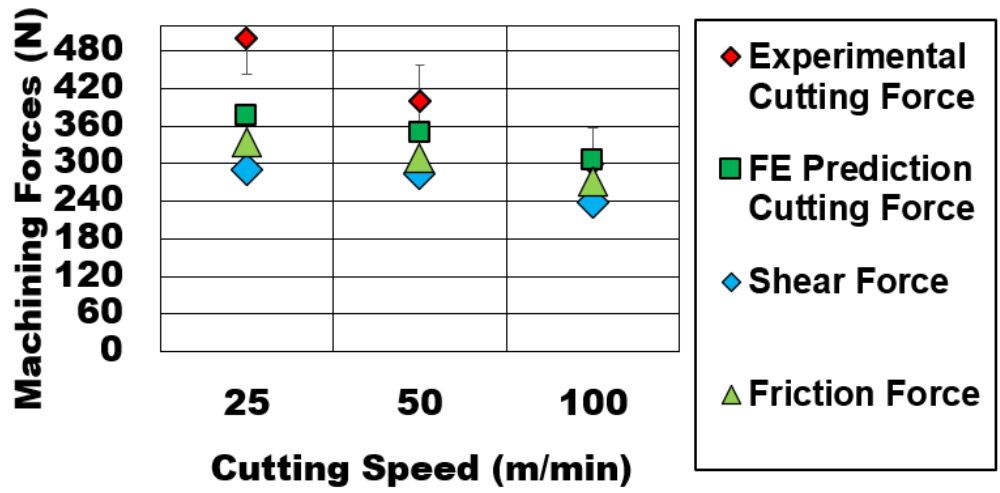
(b) AA7075 syntactic foam

Figure 13: Variation in machining forces (analytical/FE) with cutting speed: (a) AA6061, (b) AA7075; (Vp = 10%, b = 3 mm, h = 0.07 mm, dry cut)

(a)   100m/min   (d)

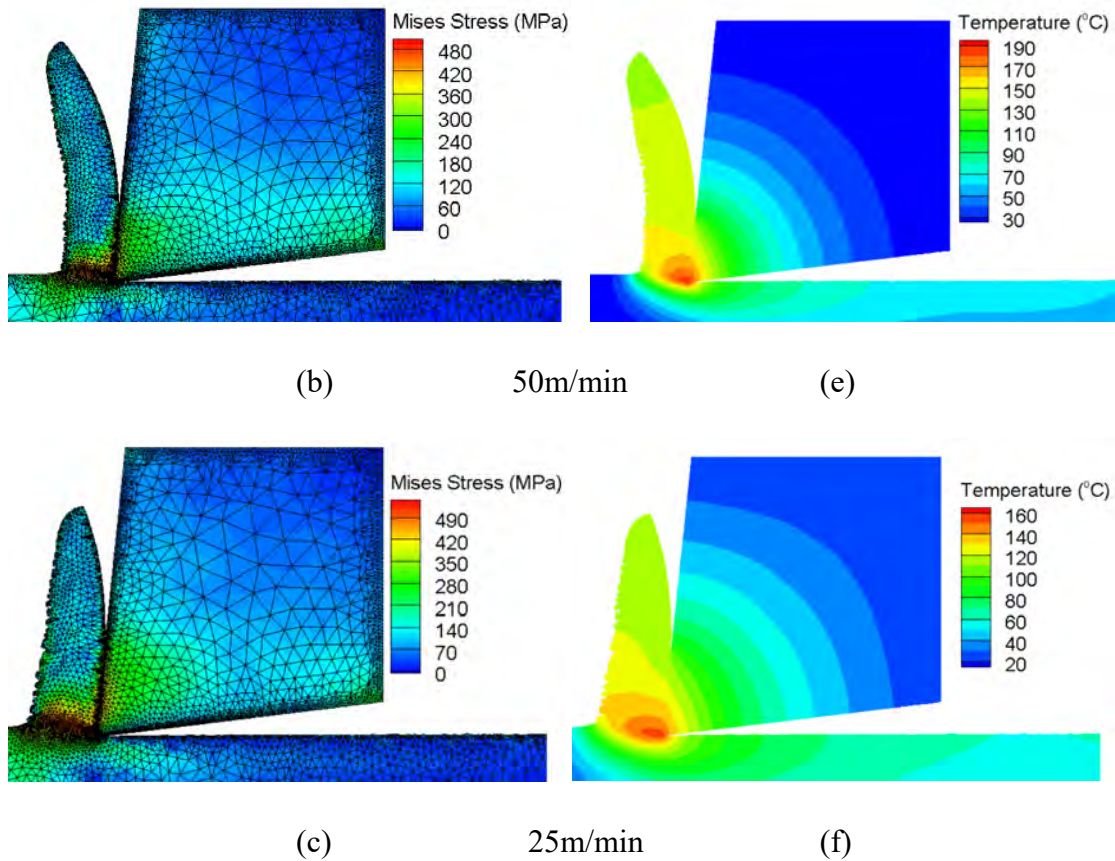(b)   50m/min   (e)

(c)   25m/min   (f)

Figure 14: Von Mises stress contour and temperature contours for AA6061-based syntactic foam: (a), (d) 100 m/min; (b), (e) 50 m/min; (c), (f) 25 m/min; (Vp = 10%, b = 3 mm, h = 0.07 mm, dry cut)

in the shear zone pinning the aluminum grains. Work hardening of the aluminum matrix with increasing feed creates the need for higher specific energy to initiate plastic deformation. The developed model was able to predict the cutting forces, with an error range of 5–10%, for the different values of feed used in this study. The proposed model was used to predict the friction forces generated due to the chip-sliding mechanisms on the tool's rake face. The FE model shows an increase in the magnitude of the friction force and normal force on the tool chip interface with an increase in the undeformed chip thickness. The chip–tool contact length increases with an increase in feed and the number of microspheres in the shear zone. In addition, the force model predictions for both two-body abrasion and three-body abrasion components of the friction force increase with feed.

6.3.   Effect of Volume Fraction and Average Size of Microspheres

The effect of the ceramic hollow alumina microsphere volume fraction and its average size on the cutting force generated is shown in Figure 19 (a) and (b). The key

48

deformation mechanisms observed during the cutting of AA6061 and AA7075 aluminum reinforced with ceramic hollow alumina microspheres were the strain hardening of the matrix that protects the microspheres in position, causing the two-body abrasion of the cutting tool. Second, the microspheres that exceeded their crushing strength burst open and resulted in a large amount of abrasive debris, leading to three-
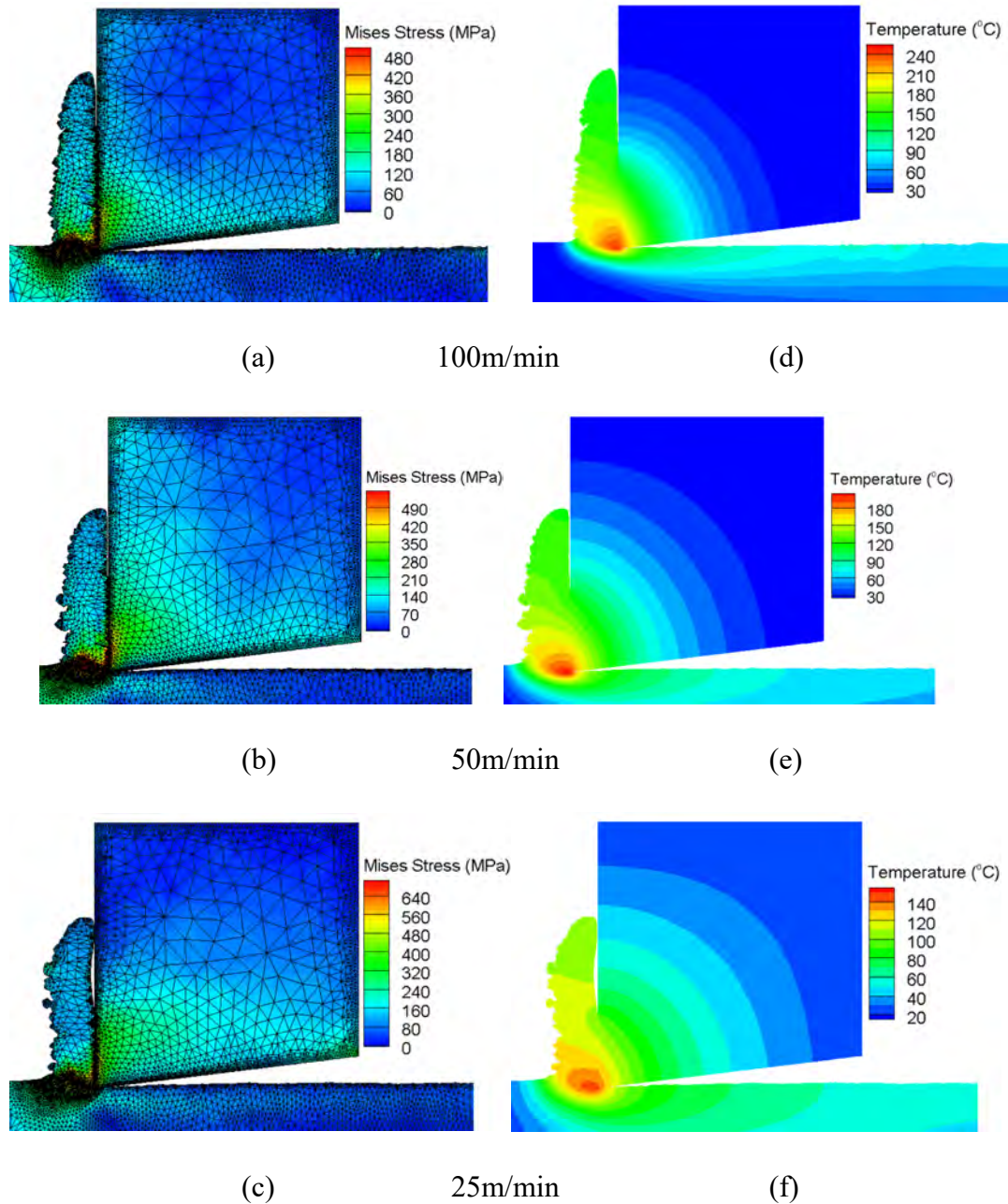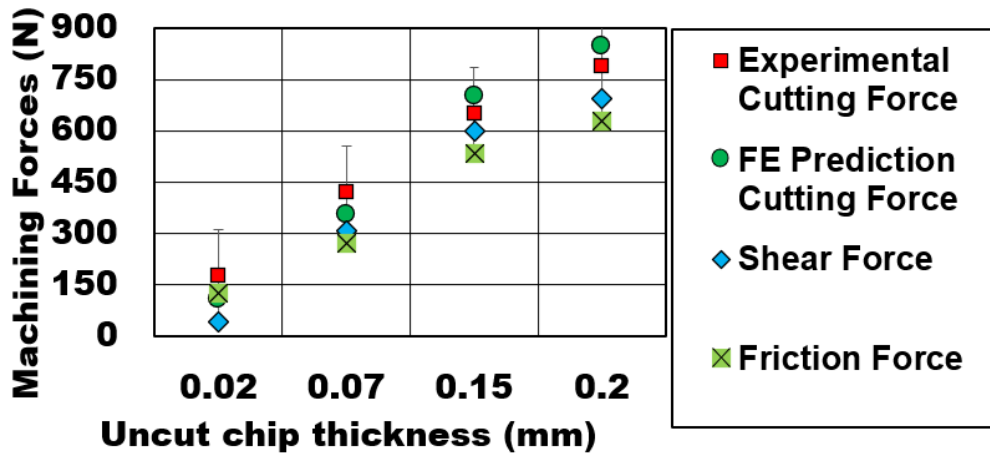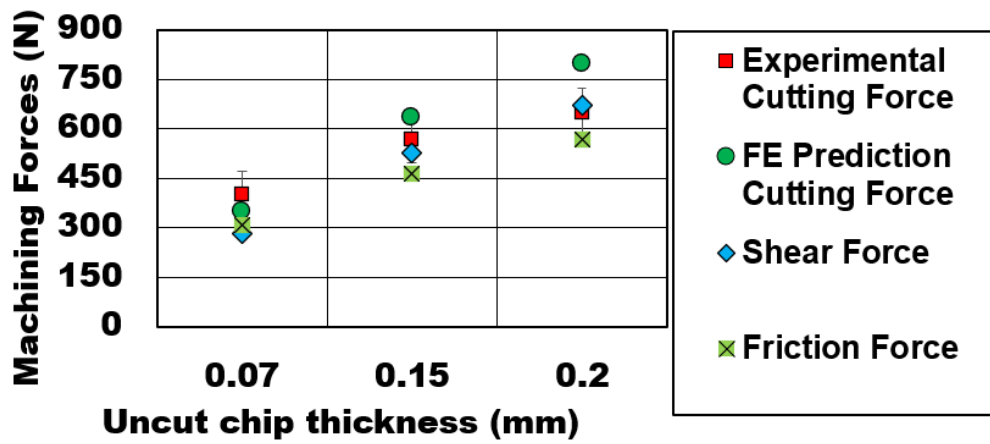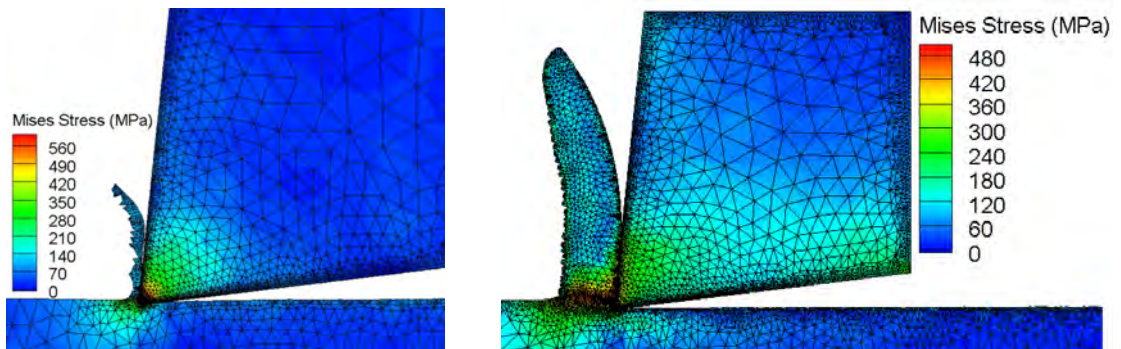

Figure 15: Von Mises stress contours and temperature contours for AA7075-based syntactic foams: (a), (d) 100 m/min; (b), (e) 50 m/min; (c), (f) 25 m/min; (Vp = 10%, b = 3 mm, h = 0.07 mm, dry cut)

(a) AA6061 syntactic foam

(b) AA7075 syntactic foam

Figure 16: Variation in the machining forces (analytical/FE) with uncut chip thickness: (a) AA6061-based syntactic foam; (b) AA7075-based syntactic foam; (Vp = 10%, b = 3 mm, 50 m/min, dry cut)

(a) h = 0.02mm

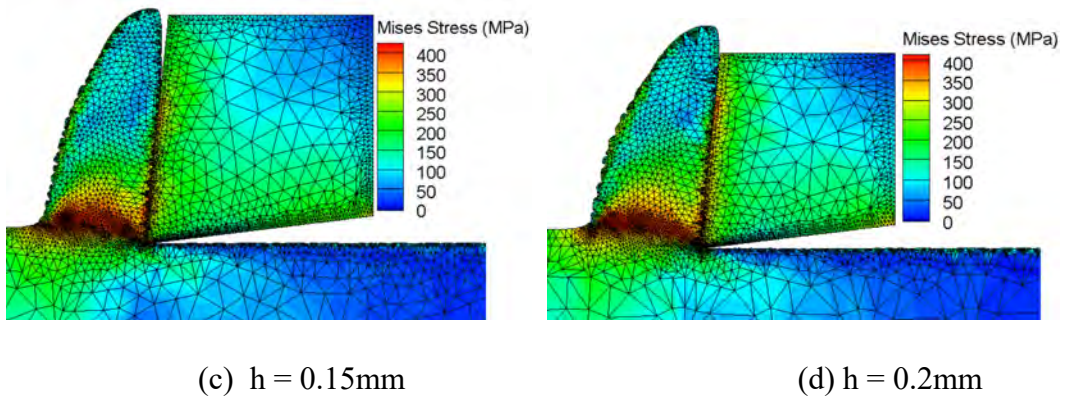(b) h = 0.07mm

(c) h = 0.15mm   (d) h = 0.2mm

Figure 17: Von Mises stress contours for AA6061-based syntactic foam: (a) h = 0.02 mm; (b) h = 0.07 mm; (c) h = 0.15 mm; (d) h = 0.2 mm; (Vp = 10%, b = 3 mm, 50 m/min, dry cut)

(a) h = 0.07mm   (b) h = 0.15mm
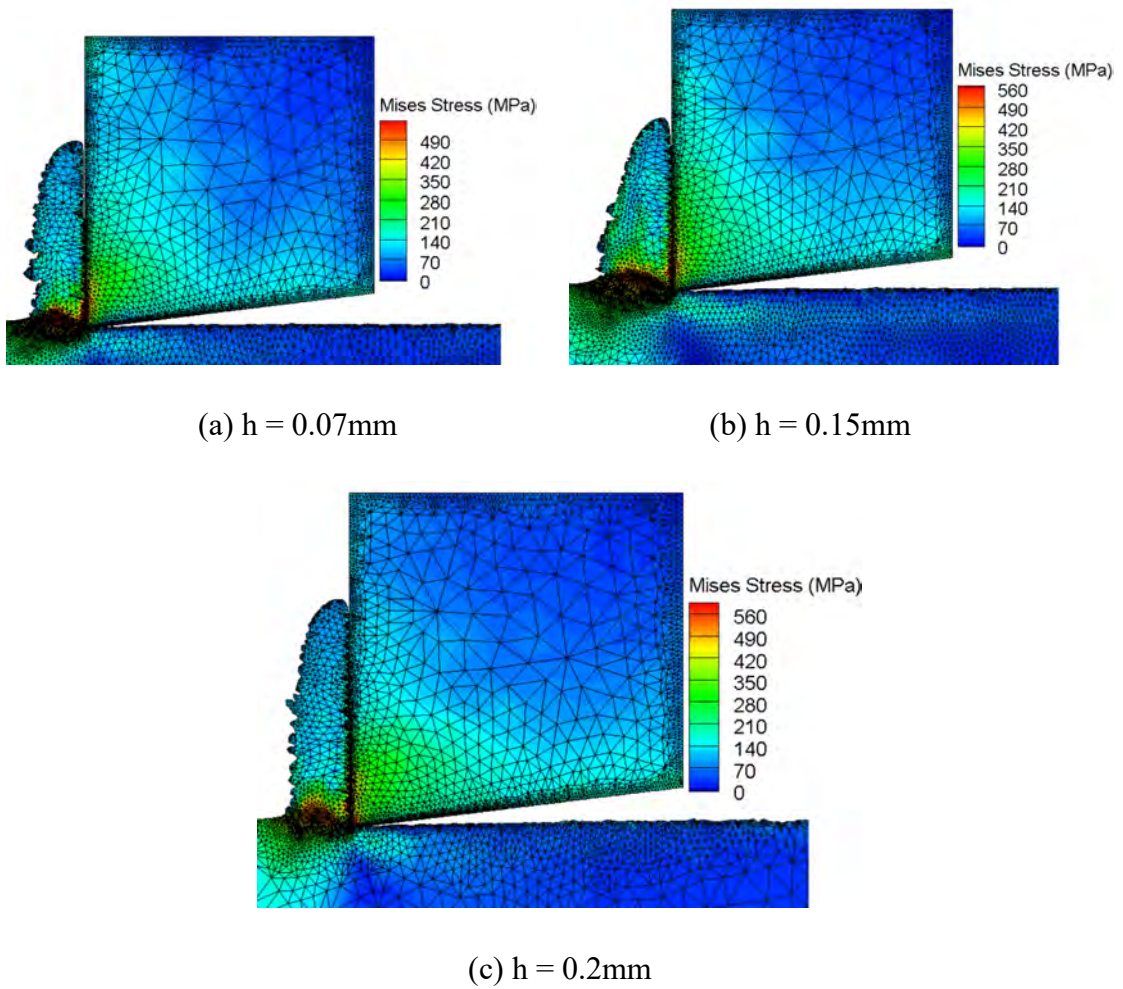
(c) h = 0.2mm

Figure 18: Von Mises stress contours for AA7075-based syntactic foam: (a) h = 0.07 mm; (b) h = 0.15mm; (c) h = 0.2 mm; (Vp = 10%, b = 3 mm, 50 m/min, dry cut)

body rolling abrasion between the sliding chip and the tool's rake face. The shear strength of the foam increases with an increase in the volume fraction of hollow microspheres. Thus, the shear force required to cause plastic deformation increases as a result. Further, an increase in the volume fraction of microspheres causes an increase in the number of hollow microspheres along the shear zone. This increases the work hardening behavior of the aluminum matrix and causes an increase in the cutting force generated (Figure 20 (a), (b) and Figure 20 (d), (e)). However, an increase in the average size of the hollow microspheres caused a drop in the cutting forces. This is attributed to a larger proportion of defects in the form of pores and micro-cracks being present in the larger microsphere size, which lead to faster defect propagation and the ultimate fracturing of the microsphere. The model was able to predict the cutting forces with an error margin of 5–10%.

Figure 19 (a) and (b) also show the variation in the friction force with an increase in the volume fraction of microspheres and their average sizes. The FE model predictions showed an increase in the friction force with an increase in the volume fraction of hollow alumina reinforcements and a slight decrease in the friction force with coarser alumina reinforcements. For the same average-sized microspheres, an increase in volume fraction led to an increase in the number of microspheres engaged in the two-body and three-abrasion mechanisms for the tool's rake face, contributing to an increase in the total friction and normal forces. However, for a fixed volume fraction,
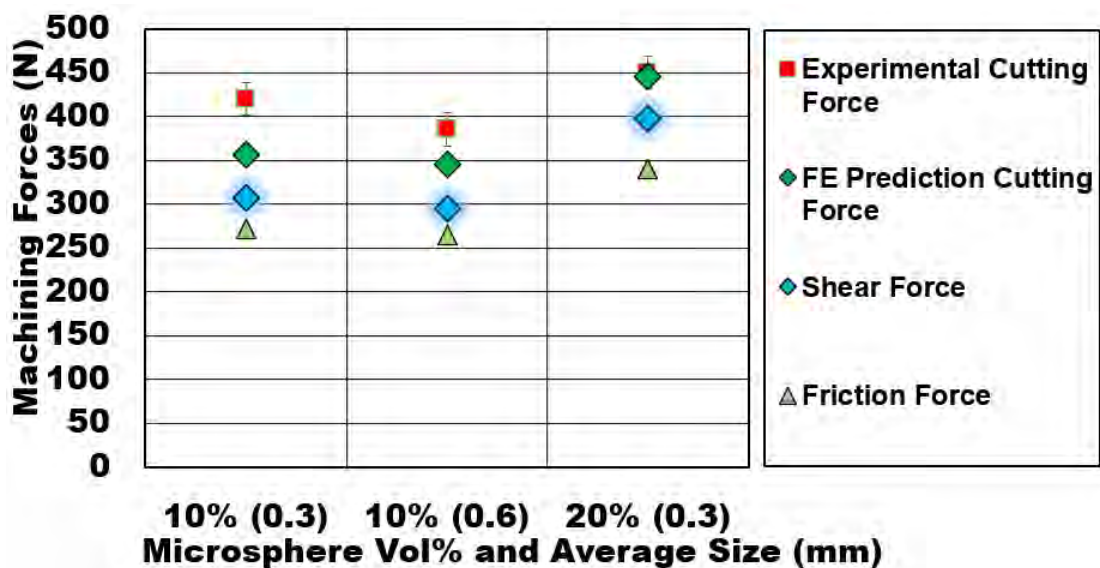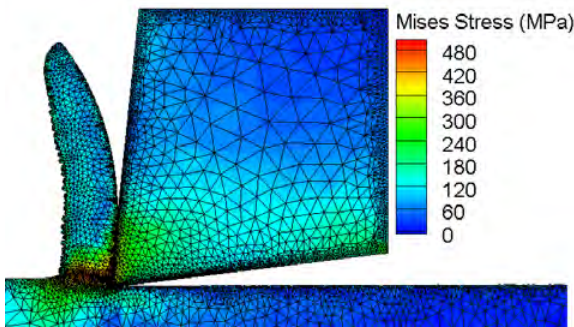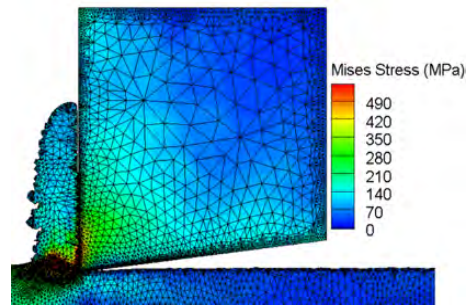

(a) AA6061 syntactic foam
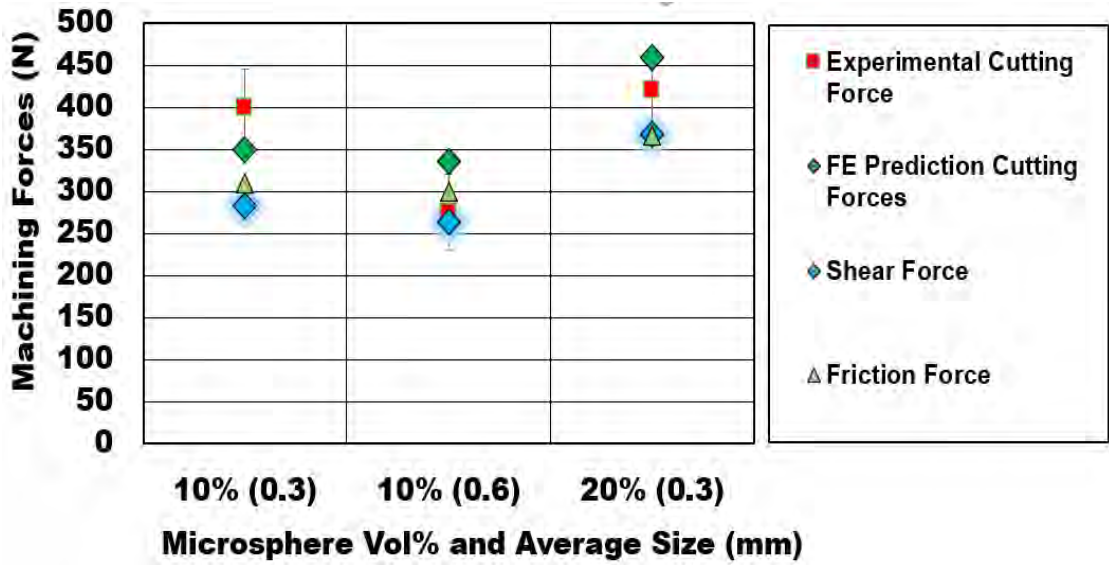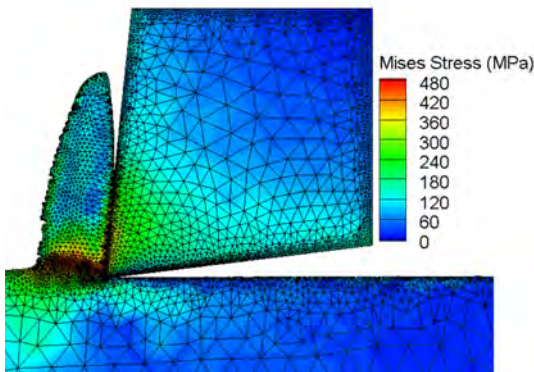
(b) AA7075 syntactic foam

Figure 19: Variation in the machining forces (analytical/FE) with volume fraction and average size of hollow microspheres for (a) AA6061-based and (b) AA7075-based syntactic foam; (50 m/min, b = 3 mm, h = 0.07 mm, dry cut)
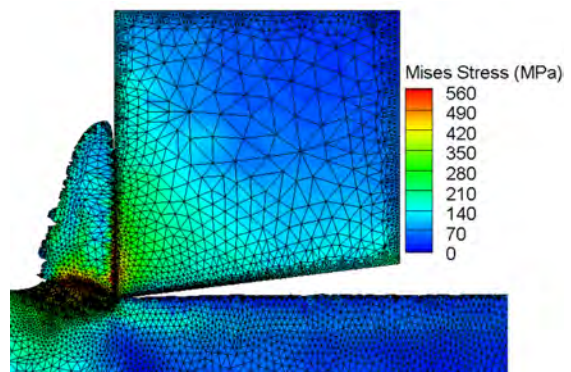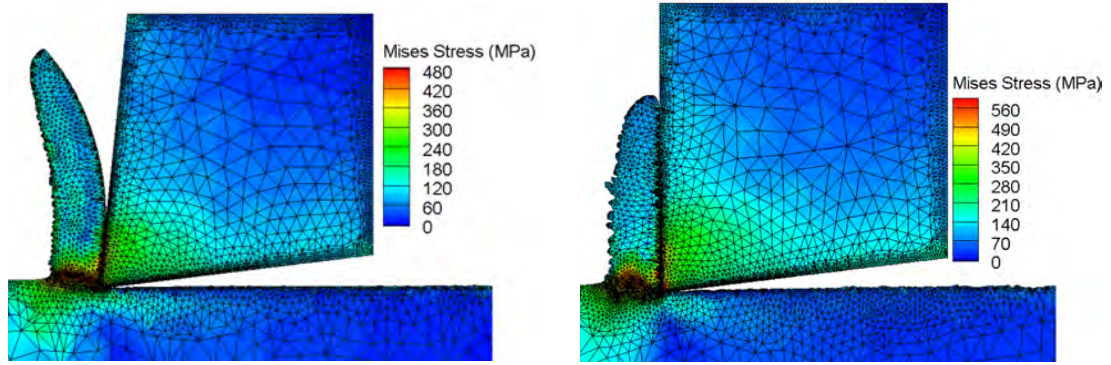

(a)   10% volume fraction, 0.3mm bubble size   (d)

(b)   20% volume fraction, 0.3mm bubble size   (e)

53

(c)   10% volume fraction, 0.6mm bubble size   (f)

Figure 20: Von Mises Stress contours for (a)–(c) AA6061-based and (d)–(f) AA7075-based syntactic foams; (a), (d) 10%, 0.3 mm; (b), (e) 20%, 0.3 mm; (c), (f) 10%, 0.6 mm; (50 m/min, b = 3 mm, h = 0.07 mm, dry cut)

it was observed that a decrease in microsphere size causes higher friction and normal forces compared to when coarser microsphere sizes are used. This points toward more active two-body abrasion due to the enhancement in the hardening behavior of the AA6061 matrix, pinned by an increase in the number of the smaller-sized microspheres. In addition, a higher number of microspheres in the matrix are also associated with a higher percentage of loose ceramic debris rolling between the chip and the tool due to crushed microspheres, thus increasing the friction force and microsphere crush force.

6.4.   Key Failure Mechanisms

In the machining of aluminum-based syntactic foams, the chip formation depends on factors such as the chip compression ratio, shear angle, and matrix transverse. During the initial stage of machining, the foam in front of the tool experiences compression from all sides. The hollow alumina microspheres in the matrix have good compressive strength. At this point, the microspheres transfer the load on to the microspheres. In this way, the hollow alumina microspheres raise the elastic stiffness of the syntactic foam. When the material reaches closer to the tip of the tool, high shear stresses are developed in the material. Further, a significant amount of heat generation is caused due to deformation in the shear zone. When the matrix starts to plastically deform, the hollow microspheres carry the load through a load transfer via the interface between the matrix and the microspheres, thereby unloading the matrix. Once the critical value of the compression force is reached, the hollow microsphere collapses and fractures, which leads to the densification of the matrix and, subsequently,

the closing of the pores. The experimental chips for AA6061- and AA7075-based syntactic foams are shown in Figure 21(a) and Figure 21(b), respectively. There are three deformation mechanisms observed from the chips formed during the machining experiments (as shown in Figure 22).

- During the chip formation, when the compressive strength of the hollow microsphere is exceeded, fracturing of the microspheres takes place.
- The matrix around the hollow microsphere starts to work-harden.
- The collapse of the hollow microspheres leads to the further plastic deformation of the matrix, resulting in matrix densification.
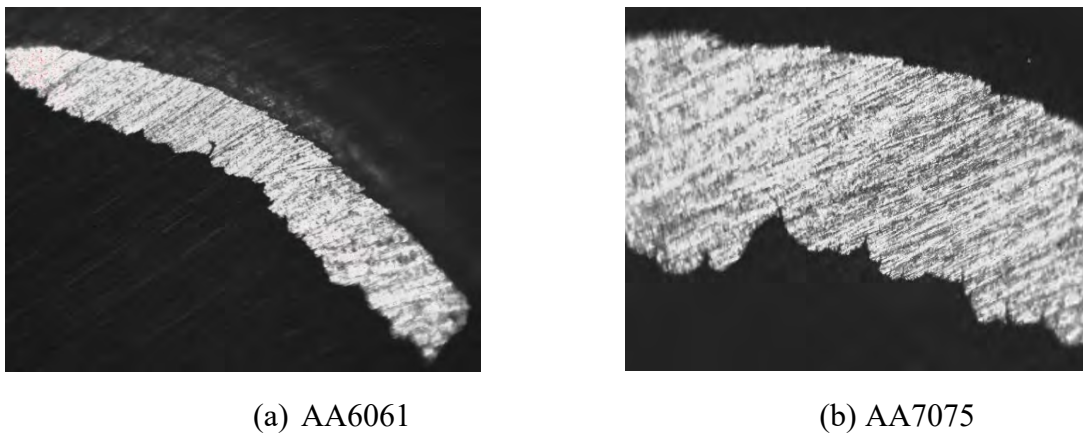

(a) AA6061   (b) AA7075

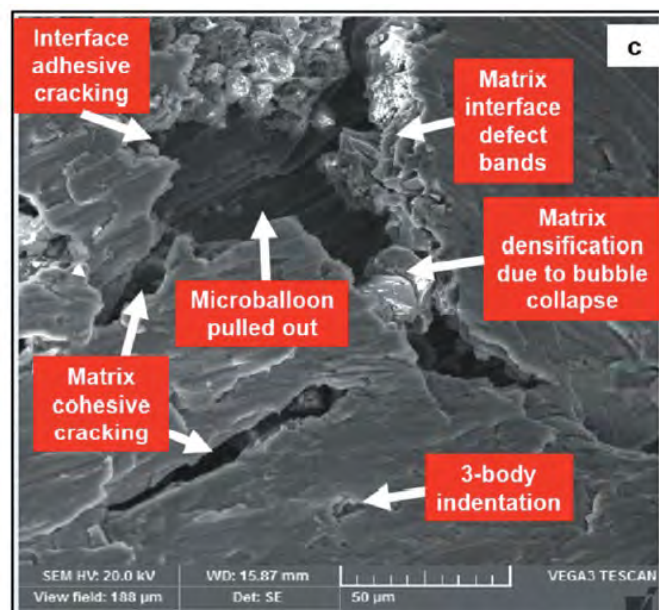Figure 21: Experimental chips of MMSF

Figure 22: Deformation mechanisms for syntactic foam [50]

6.5. Fracture Mechanism of Hollow Microsphere

There are two modes for a hollow microsphere fracture (see Figure 23):

- The hollow microsphere present in the chip gets fractured and collapses as it passes through the shear zone, which leads to matrix densification. This type of fracture is of the Mode-1 type.
- When the hollow microsphere is located in front of the cutting tool, the bubble gets sheared into two parts. This type of fracture is of the Mode-2 type.
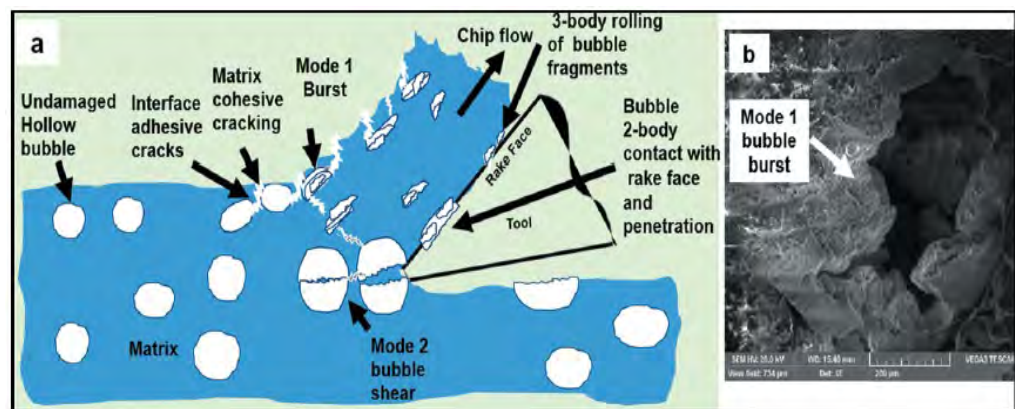

Figure 23: Modes of hollow microsphere fractures

There are three types of hollow microsphere fracture mechanisms that can potentially contribute to the continuation of crack propagation.

- Case 1: Bubble in the workpiece
- Case 2: Bubble in front of the cutting tool
- Case 3: Bubble in the chip

The first type of fracture (see Figure 24) is related to the interfacial debonding of the hollow microspheres, which causes a part of the microsphere to get pulled out from the aluminum matrix and leaves a hollow cavity. Alternatively, the interface cracking makes the fractured microsphere sink deeper into the matrix. The second type of fracture (see Figure 25) is caused when the cutting tool shears the hollow microsphere, since its shear strength is lower in comparison to the compressive strength, thus leading to the shear failure of microspheres. The third type of failure (see Figure 26) occurs when the compressive energy supplied by the cutting tool on the surface of the microsphere causes the microsphere fracture. This transfers the load back
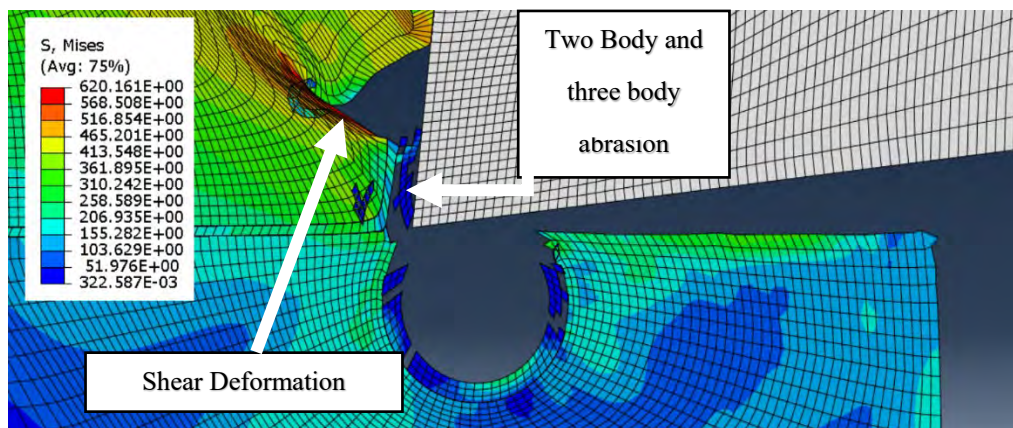
to the matrix to further crush the microsphere, thereby leading to the densification phase, as the foam undergoes intense shear deformation.
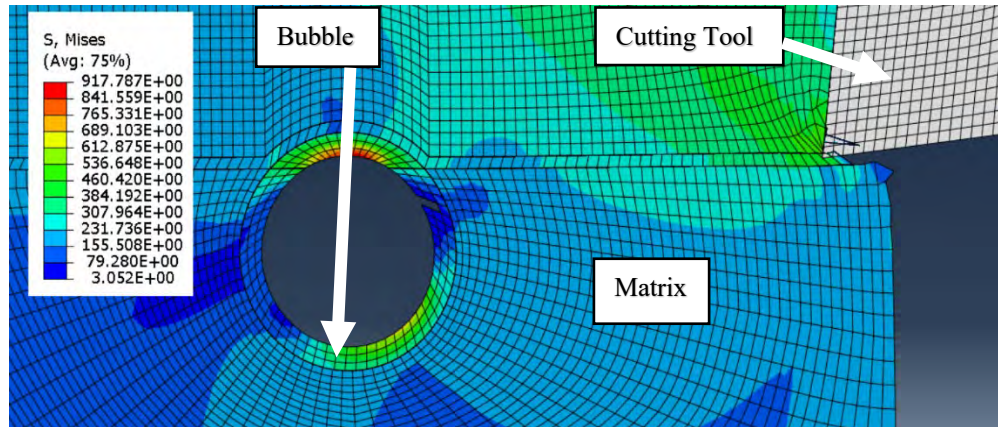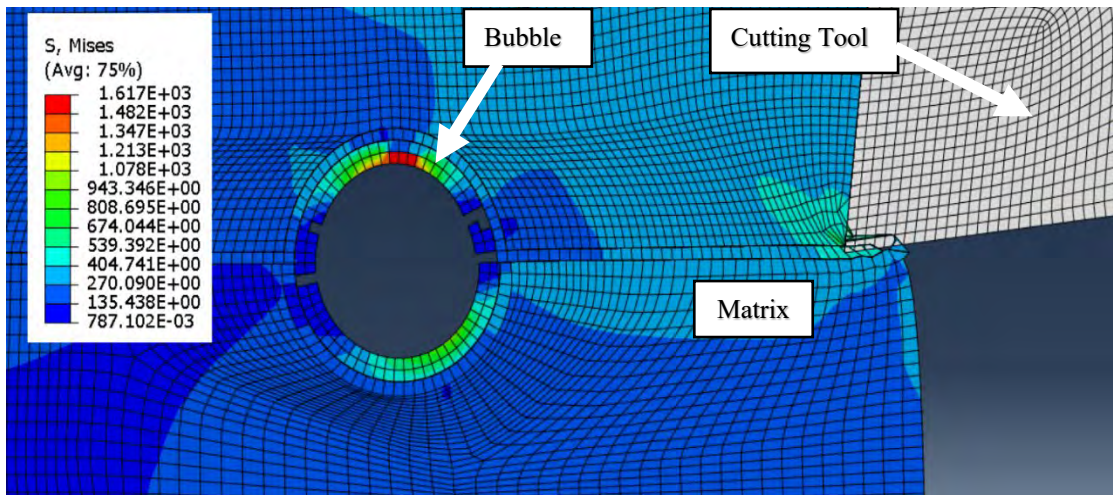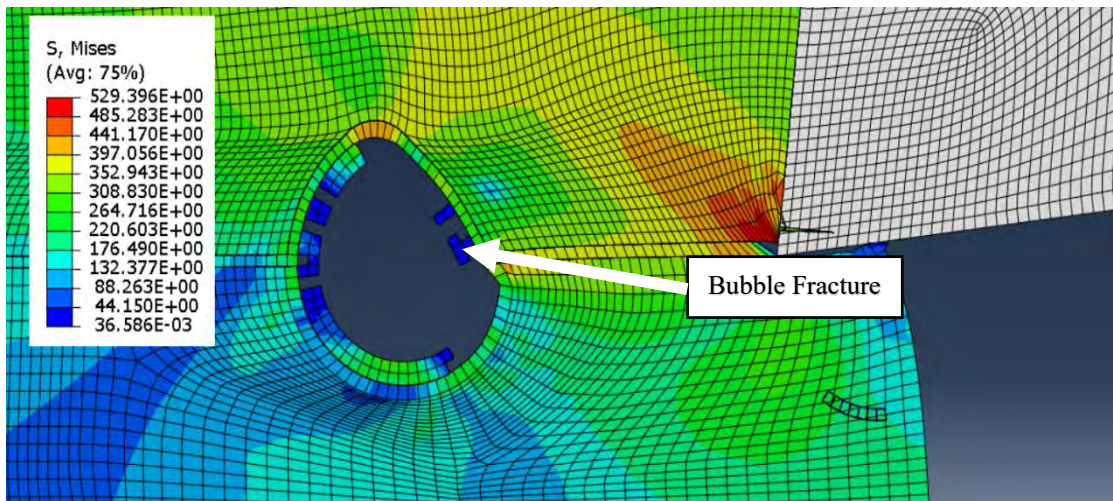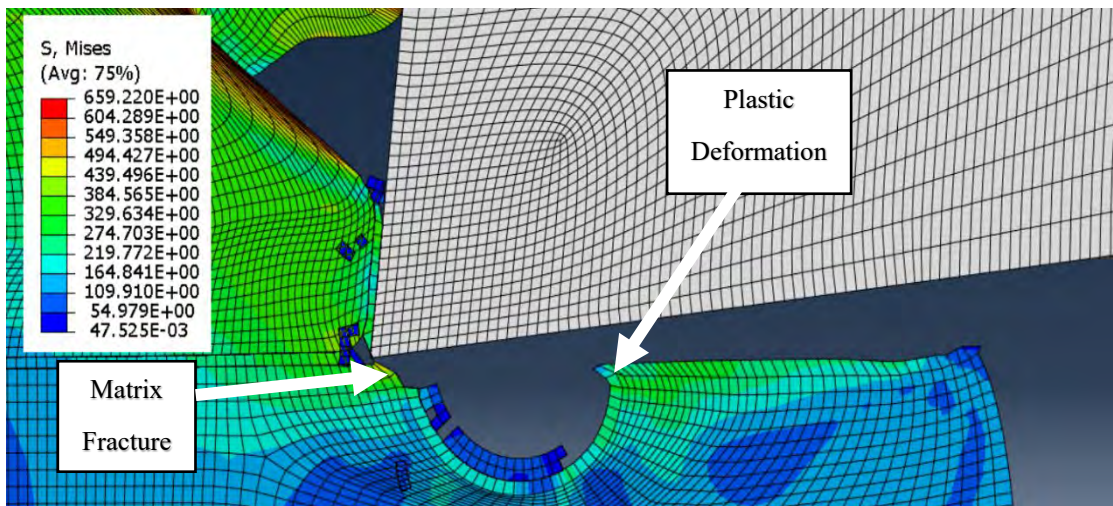

(a)
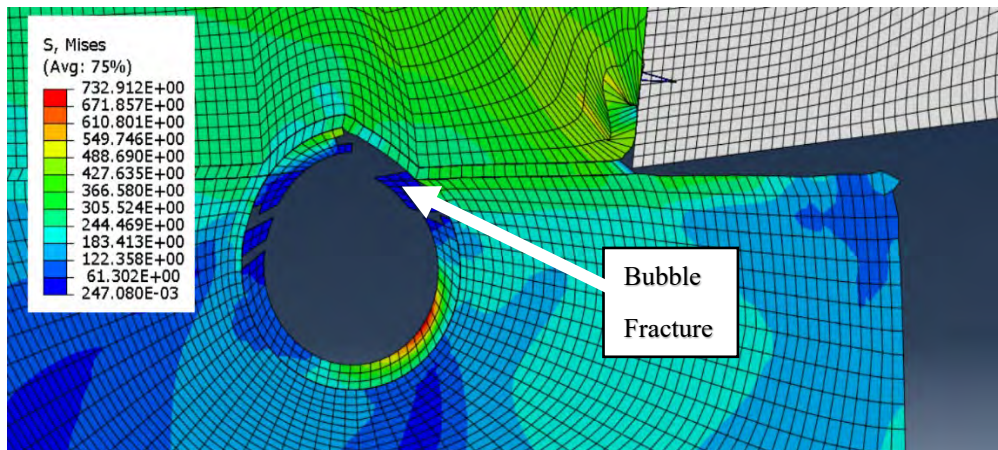
(b)

(c)

Figure 24: Effect of hollow microspheres in the workpiece
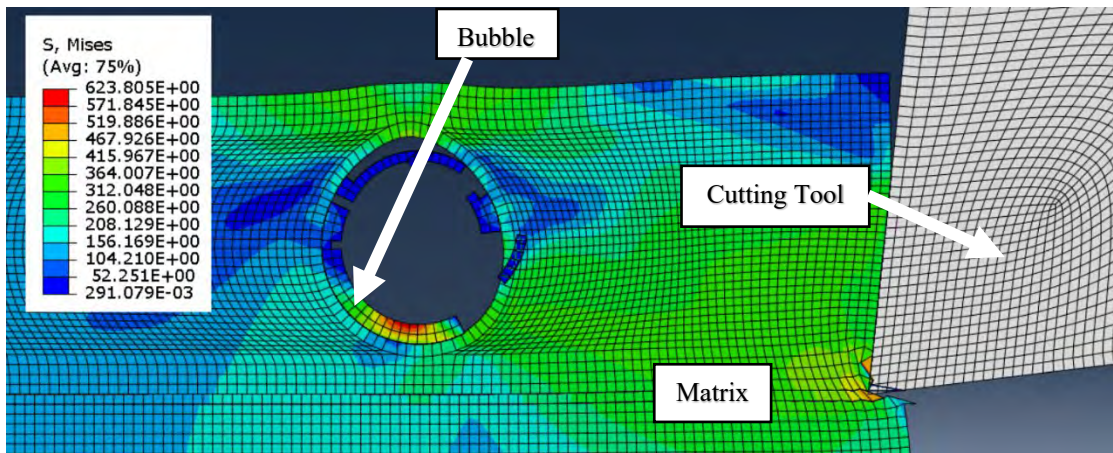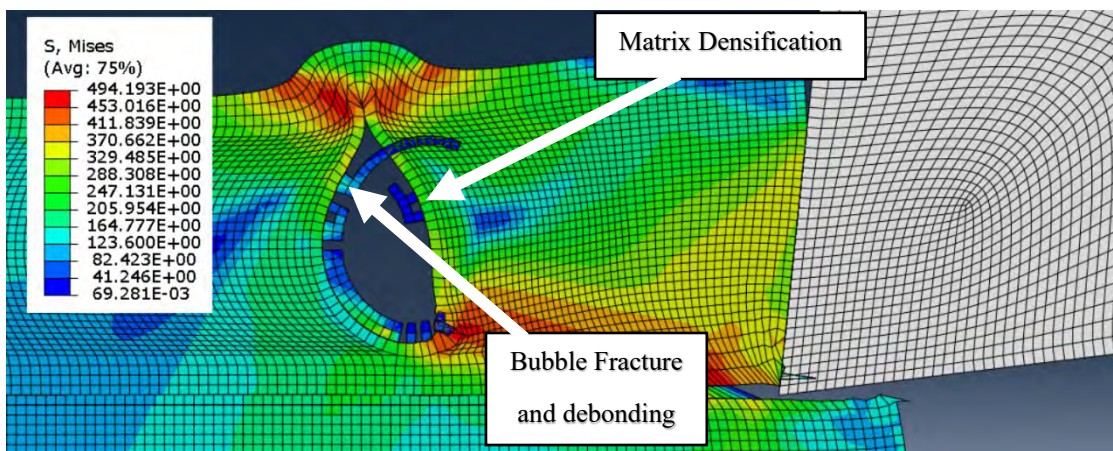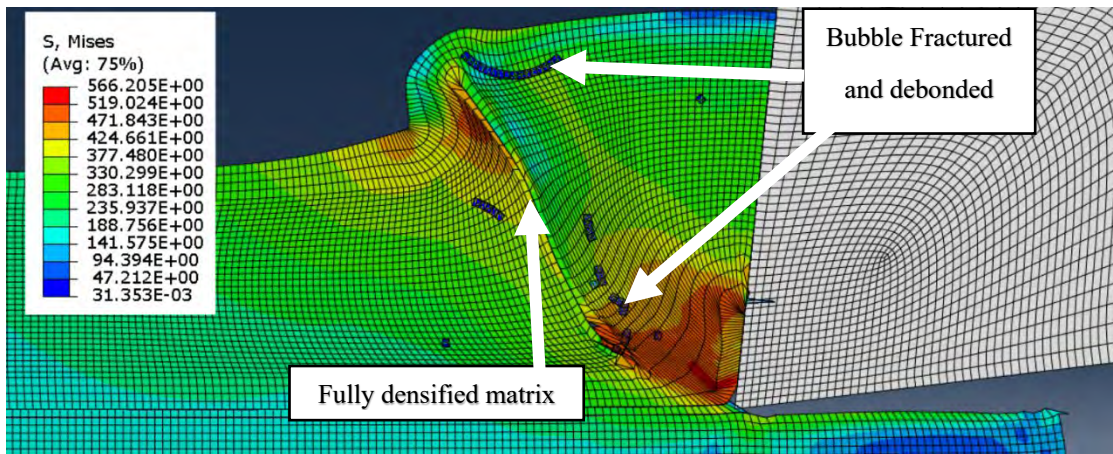
(a)

(b)

(c)

Figure 25: Effect of hollow microspheres in front of the cutting tool

(a)

(b)

(c)

Figure 26: Effect of hollow microspheres in the chip

Chapter 7. Conclusion

In this thesis, a 2-D thermo-mechanical FE model has been developed using the AdvantEdge^{TM} software, developed by Third Wave Systems, for simulating the cutting forces generated during the orthogonal machining of AA6061- and AA7075-based syntactic foams. From this model, the following conclusions were obtained:

- The cutting force decreased by 33% with an increase in the cutting speed due to the thermal softening of the aluminum matrix.

- An increase in undeformed chip thickness caused the cutting forces to increase tremendously. This is due to the increasing chip load created by the increase in feed.

- An increase in the average hollow-bubble size results in a decrease in the cutting force by 25%. With an increase in the volume fraction, the number of bubbles in the primary shear zone increases, leading to the higher shear strength of the aluminum matrix. This causes an increase in the cutting force.

- An increase in the average hollow-bubble size results in a decrease in the cutting forces by 3%. The coarser the bubble size is, the more significant the surface defects are. Hence, the bubble fractures that occur at a lower crush strength lead to a reduction in the cutting force.

- The disintegrated bubbles contribute to the two-body and three-body abrasion of the hollow microspheres on the rake face, resulting in a higher friction force. This is particularly pronounced with a higher volume fraction of microspheres in the syntactic foams.

A 2-D heterogeneous model was developed using ABAQUS/Explicit to explain the failure mechanisms that contribute to chip formation. It has been shown through the ABAQUS simulation that the location of the hollow microspheres significantly affects the generation of peak cutting forces by altering the plastic deformation characteristics of the aluminum matrix. The developed FE model, constructed using the AdvantEdge^{TM} software, was capable of predicting the cutting forces with a 15% error margin as compared to the experimentally measured forces.

References

[1] R. R. Nagavally, "Composite materials-history, types, fabrication techniques, advantages, and applications," *Int. J. Mech. Prod. Eng.*, vol. 5, no. 9, pp. 82–87, 2017.

[2] K. K. Chawla, "Metal Matrix Composites," in *Composite Materials: Science and Engineering*, New York, NY: Springer New York, 2012, pp. 197–248.

[3] S. Kannan and H. A. Kishawy, "Tribological aspects of machining aluminium metal matrix composites," *J. Mater. Process. Technol.*, vol. 198, no. 1, pp. 399–406, 2008, doi: https://doi.org/10.1016/j.jmatprotec.2007.07.021.

[4] V. Ramnath *et al.*, "Aluminium metal matrix composites - A review," *Rev. Adv. Mater. Sci.*, vol. 38, pp. 55–60, Aug. 2014.

[5] M. Shukla, S. K. Dhakad, P. Agarwal, and M. K. Pradhan, "Characteristic behaviour of aluminium metal matrix composites: A review," *Mater. Today Proc.*, vol. 5, no. 2, Part 1, pp. 5830–5836, 2018, doi: https://doi.org/10.1016/j.matpr.2017.12.180.

[6] H. Ye and X. Y. Liu, "'Review of Recent Studies in Magnesium Matrix Composites,'" *J. Mater. Sci.*, vol. 39, pp. 6153–6171, Jan. 2004, doi: 10.1023/B:JMSC.0000043583.47148.31.

[7] S. Sarapure, B. Satish, G. Bm, and . B., "Microstructure and Mechanical Behavior of Magnesium Alloy AZ91 Hybrid Composites," *IOP Conf. Ser. Mater. Sci. Eng.*, vol. 310, p. 12161, Feb. 2018, doi: 10.1088/1757-899X/310/1/012161.

[8] M. P. Groover, *Principles of modern manufacturing LK - https://aus.on.worldcat.org/oclc/645588607*, 4th ed., S. Hoboken, N.J. SE - xiv, 1002 pages : illustrations ; 26 cm + 1 DVD: J. Wiley & Sons, 2011.

[9] E. M. Trent and P. K. Wright, "Chapter 1 - Introduction: Historical and economic context," in *Metal Cutting (Fourth Edition)*, Fourth Edi., E. M. Trent and P. K. Wright, Eds. Woburn: Butterworth-Heinemann, 2000, pp. 1–8.

[10] M. Seeman, G. Ganesan, R. Karthikeyan, and A. Velayudham, "Study on tool wear and surface roughness in machining of particulate aluminum metal matrix composite-response surface methodology approach," *Int. J. Adv. Manuf. Technol.*, vol. 48, no. 5, pp. 613–624, 2010, doi: 10.1007/s00170-009-2297-z.

[11] A. Pramanik and L. C. Zhang, "Particle fracture and debonding during orthogonal machining of metal matrix composites," *Adv. Manuf.*, vol. 5, no. 1, pp. 77–82, 2017, doi: 10.1007/s40436-017-0170-0.

[12] C. R. Dandekar and Y. C. Shin, "Modeling of machining of composite materials: A review," *Int. J. Mach. Tools Manuf.*, vol. 57, pp. 102–121, 2012, doi: https://doi.org/10.1016/j.ijmachtools.2012.01.006.

[13] S.-J. Park and M.-K. Seo, "Chapter 7 - Types of Composites," in *Interface Science and Composites*, vol. 18, S.-J. Park and M.-K. Seo, Eds. Elsevier, 2011,

pp. 501–629.

[14] M. Ali, R. Rubel, and S. Yusuf, "A review on syntactic foams processing, preparation and applications," in *International Conference on Mechanical Engineering and Renewable Energy*, 2019.

[15] S. Sankaran, B. N. Ravishankar, K. Ravi Sekhar, S. Dasgupta, and M. N. Jagdish Kumar, "Syntactic Foams for Multifunctional Applications: Datasheet from · Volume : 'Composite Materials' in SpringerMaterials (https://doi.org/10.1007/978-3-662-49514-8_9)." Springer-Verlag Berlin Heidelberg.

[16] P. K. Rohatgi, N. Gupta, B. F. Schultz, and D. D. Luong, "The synthesis, compressive properties, and applications of metal matrix syntactic foams," *JOM*, vol. 63, no. 2, pp. 36–42, 2011, doi: 10.1007/s11837-011-0026-1.

[17] P. S. Liu and G. F. Chen, "Chapter Three - Application of Porous Metals," in *Porous Materials*, P. S. Liu and G. F. Chen, Eds. Boston: Butterworth-Heinemann, 2014, pp. 113–188.

[18] I. N. Orbulov, A. Kemény, Á. Filep, and Z. Gácsi, "Compressive characteristics of bimodal aluminium matrix syntactic foams," *Compos. Part A Appl. Sci. Manuf.*, vol. 124, p. 105479, 2019, doi: https://doi.org/10.1016/j.compositesa.2019.105479.

[19] S. Broxtermann, M. Taherishargh, I. V Belova, G. E. Murch, and T. Fiedler, "On the compressive behaviour of high porosity expanded Perlite-Metal Syntactic Foam (P-MSF)," *J. Alloys Compd.*, vol. 691, pp. 690–697, 2017, doi: https://doi.org/10.1016/j.jallcom.2016.08.284.

[20] D. Newsome, B. Schultz, J. B. Ferguson, and P. Rohatgi, "Synthesis and Quasi-Static Compressive Properties of Mg-AZ91D-Al2O3 Syntactic Foams," *Materials (Basel).*, vol. 8, pp. 6085–6095, Nov. 2015, doi: 10.3390/ma8095292.

[21] M. Kiser, M. Y. He, and F. W. Zok, "The mechanical response of ceramic microballoon reinforced aluminum matrix composites under compressive loading," *Acta Mater.*, vol. 47, no. 9, pp. 2685–2694, 1999, doi: https://doi.org/10.1016/S1359-6454(99)00129-9.

[22] G. H. Wu, Z. Y. Dou, D. L. Sun, L. T. Jiang, B. S. Ding, and B. F. He, "Compression behaviors of cenosphere–pure aluminum syntactic foams," *Scr. Mater.*, vol. 56, no. 3, pp. 221–224, 2007, doi: https://doi.org/10.1016/j.scriptamat.2006.10.008.

[23] D. K. Balch and D. C. Dunand, "Load partitioning in aluminum syntactic foams containing ceramic microspheres," *Acta Mater.*, vol. 54, no. 6, pp. 1501–1511, 2006.

[24] D. P. Mondal *et al.*, "Titanium-cenosphere syntactic foam made through powder metallurgy route," *Mater. Des.*, vol. 34, pp. 82–89, 2012, doi: https://doi.org/10.1016/j.matdes.2011.07.055.

[25] J. B. Ferguson, J. A. Santa Maria, B. F. Schultz, and P. K. Rohatgi, "Al–Al2O3 syntactic foams—Part II: Predicting mechanical properties of metal matrix

syntactic foams reinforced with ceramic spheres," *Mater. Sci. Eng. A*, vol. 582, pp. 423–432, 2013, doi: https://doi.org/10.1016/j.msea.2013.06.065.

[26]   A. Pramanik, L. C. Zhang, and J. A. Arsecularatne, "An FEM investigation into the behavior of metal matrix composites: Tool–particle interaction during orthogonal cutting," *Int. J. Mach. Tools Manuf.*, vol. 47, no. 10, pp. 1497–1506, 2007, doi: https://doi.org/10.1016/j.ijmachtools.2006.12.004.

[27]   Q. Wu, W. Xu, and L. Zhang, "A micromechanics analysis of the material removal mechanisms in the cutting of ceramic particle reinforced metal matrix composites," *Mach. Sci. Technol.*, vol. 22, no. 4, pp. 638–651, 2018, doi: 10.1080/10910344.2017.1382516.

[28]   U. Umer, H. Kishawy, A. Ghandehariun, L. Xie, and A. Al-Ahmari, "On modeling tool performance while machining aluminum-based metal matrix composites," *Int. J. Adv. Manuf. Technol.*, vol. 92, no. 9, pp. 3519–3530, 2017, doi: 10.1007/s00170-017-0368-0.

[29]   M. G. Elkhateeb and Y. C. Shin, "Investigation of the Machining Behavior of Ti6Al4V/TiC Composites During Conventional and Laser-Assisted Machining," *J. Manuf. Sci. Eng.*, vol. 141, no. 5, Mar. 2019, doi: 10.1115/1.4042608.

[30]   T. Dou, H. Fu, Z. Li, X. Ji, and S. Bi, "Prediction model, simulation, and experimental validation on thrust force and torque in drilling SiCp/Al6063," *Int. J. Adv. Manuf. Technol.*, vol. 103, no. 1, pp. 165–175, 2019, doi: 10.1007/s00170-019-03366-1.

[31]   U. Umer, M. H. Abidi, J. A. Qudeiri, and H. Alkhalefah, "Evaulation of a equivalent homogeneous material model while machining aluminum based metal matrix composite," *Mater. Today Proc.*, no. xxxx, 2020, doi: 10.1016/j.matpr.2020.10.679.

[32]   Q. Wu, W. Xu, and L. Zhang, "Machining of particulate-reinforced metal matrix composites: An investigation into the chip formation and subsurface damage," *J. Mater. Process. Technol.*, vol. 274, no. February, 2019, doi: 10.1016/j.jmatprotec.2019.116315.

[33]   X. Teng, D. Huo, W. Chen, E. Wong, L. Zheng, and I. Shyha, "Finite element modelling on cutting mechanism of nano Mg/SiC metal matrix composites considering cutting edge radius," *J. Manuf. Process.*, vol. 32, pp. 116–126, 2018, doi: 10.1016/j.jmapro.2018.02.006.

[34]   U. Umer, M. Ashfaq, J. A. Qudeiri, H. M. A. Hussein, S. N. Danish, and A. R. Al-Ahmari, "Modeling machining of particle-reinforced aluminum-based metal matrix composites using cohesive zone elements," *Int. J. Adv. Manuf. Technol.*, vol. 78, no. 5–8, pp. 1171–1179, 2015, doi: 10.1007/s00170-014-6715-5.

[35]   H. Pen, J. Guo, Z. Cao, X. Wang, and Z. Wang, "Finite element simulation of the micromachining of nanosized-silicon-carbide-particle reinforced composite materials based on the cohesive zone model," *Nami Jishu yu Jingmi Gongcheng/Nanotechnology Precis. Eng.*, vol. 1, no. 4, pp. 242–247, 2018, doi: 10.1016/j.npe.2018.12.003.

[36]   R. A. Laghari, J. Li, and W. Yongxiang, "Study of machining process of sicp/al

particle reinforced metal matrix composite using finite element analysis and experimental verification," *Materials (Basel).*, vol. 13, no. 23, pp. 1–39, 2020, doi: 10.3390/ma13235524.

[37]   R. Guerra Silva, U. Teicher, A. Nestler, and A. Brosius, "Finite element modeling of chip separation in machining cellular metals," *Adv. Manuf.*, vol. 3, no. 1, pp. 54–62, 2015, doi: 10.1007/s40436-015-0099-0.

[38]   M. Heidari and J. Yan, "Ultraprecision surface flattening of porous silicon by diamond turning," *Precis. Eng.*, vol. 49, pp. 262–277, 2017, doi: https://doi.org/10.1016/j.precisioneng.2017.02.015.

[39]   M. Heidari and J. Yan, "Material removal mechanism and surface integrity in ultraprecision cutting of porous titanium," *Precis. Eng.*, vol. 52, pp. 356–369, 2018, doi: https://doi.org/10.1016/j.precisioneng.2018.01.014.

[40]   M. Heidari, J. Akbari, and J. Yan, "Effects of tool rake angle and tool nose radius on surface quality of ultraprecision diamond-turned porous silicon," *J. Manuf. Process.*, vol. 37, pp. 321–331, 2019, doi: https://doi.org/10.1016/j.jmapro.2018.12.003.

[41]   G. Silva, U. Teicher, Brosius, and Ihlenfeldt, "2D Finite Element Modeling of the Cutting Force in Peripheral Milling of Cellular Metals," *Materials (Basel).*, vol. 13, p. 555, Jan. 2020, doi: 10.3390/ma13030555.

[42]   S. Kannan, H. A. Kishawy, S. Pervaiz, K. Thomas, R. Karthikeyan, and R. Arunachalam, "Machining of novel AA7075 foams containing thin-walled ceramic bubbles," *Mater. Manuf. Process.*, vol. 35, no. 16, pp. 1812–1821, Dec. 2020, doi: 10.1080/10426914.2020.1802038.

[43]   K. Thomas, S. Kannan, S. Pervaiz, M. Nazzal, and R. Karthikeyan, "Study on Influence of hollow ceramic microballoons on machining characteristics of 6061 aluminium metal syntactic foams- Finite Element Modeling," 2021. (Submitted)

[44]   A. Ghandehariun, M. Nazzal, H. A. Kishawy, and U. Umer, "On modeling the deformations and tool-workpiece interactions during machining metal matrix composites," *Int. J. Adv. Manuf. Technol.*, vol. 91, no. 5–8, pp. 1507–1516, 2017, doi: 10.1007/s00170-016-9776-9.

[45]   "Aluminum 6061-T6; 6061-T651." [Online]. Available: http://www.matweb.com/search/datasheet_print.aspx?matguid=1b8c06d0ca7c4 56694c7777d9e10be5b. [Accessed: 18-Apr-2021].

[46]   A. M. Rajendran and D. J. Grove, "Modeling of shock and impact behaviors of aluminum oxide," *Trans. Built Environ.*, vol. 32, pp. 447–460, 1998.

[47]   G. E. J. Poinern, N. Ali, X. Le, and D. Fawcett, "Nano-hardness and elastic modulus of anodic aluminium oxide based Poly (2-hydroxyethylmethacrylate) composite membranes," *AIMS Mater. Sci.*, vol. 1, no. 3, pp. 159–173, 2014, doi: 10.3934/matersci.2014.3.159.

[48]   A. S. Kurlov and A. I. Gusev, "Tungsten Carbides: Structure, Properties and Application in Hardmetals," *Springer Ser. Mater. Sci.*, vol. 184, 2013, doi: 10.1007/978-3-319-00524-9.

[49]   P. J. Blau, *Wear of Materials*. Elsevier, 2003.

[50]   S. Kannan, S. Pervaiz, R. J. Klassen, D. Huo, and M. Haghshenas, "An Energy-Based Analysis for Machining Novel AZ91 Magnesium Composite Foam Dispersed With Ceramic Microspheres," *J. Manuf. Sci. Eng.*, vol. 143, no. 3, pp. 1–10, 2021, doi: 10.1115/1.4048438.

Appendix A

Table 13: Errors encountered during simulation in ABAQUS and the corresponding fixes

Bugs encountered during the simulation	Fix
The simulation takes more time than needed	• Try removing the cohesive elements • Double-check the property values
Excessively distorted elements	• Adjust the location of the bubbles • Adjust mass scaling • ALE (if needed)
Error in ABAQUS license	• Adjustment of parallelization
Runtime exception has occurred	• Adjustment of parallelization • Send a screenshot of the bug to the AUS IT service desk
Parts/elements without temperature degrees of freedom	• Double-check the element type as coupled temperature–displacement for all the parts created
Section assigned to the part is not cohesive and elements are not cohesive	• Make sure the section type and the element type are cohesive

Journal Papers

[1] S. Kannan, H. A. Kishawy, S. Pervaiz, K. Thomas, R. Karthikeyan, and R. Arunachalam, "Machining of novel AA7075 foams containing thin-walled ceramic bubbles," *Mater. Manuf. Process.*, vol. 35, no. 16, pp. 1812–1821, Dec. 2020, doi: 10.1080/10426914.2020.1802038.

[2] K. Thomas, S. Kannan, S. Pervaiz, M. Nazzal, and R. Karthikeyan, "Study on Influence of hollow ceramic microballoons on machining characteristics of 6061 aluminium metal syntactic foams- Finite Element Modeling," 2021. (Submitted)

Vita

Kevin Koshy Thomas was born in 1996, in Dubai, United Arab Emirates. He underwent his primary and secondary education in Sharjah, UAE. He completed his B.Sc. degree in Mechanical Engineering from the Mahatma Gandhi University in 2018.

In September 2019, he joined the Mechanical Engineering master's program at the American University of Sharjah. During the course of his master's degree, he co-authored a paper that was published in Taylor and Francis Publications. His research interests lie in materials, design, and finite element analysis.